VU Research Portal

The effect of convergence angle on the kinematic evolution of strain partitioning in transpressional brittle wedges: Insight from analog modeling and high-resoluiton digital image analysis

Leever, K.A.; Gabrielsen, R.H.; Sokoutis, D.; Willingshofer, E.

document version
Publisher's PDF, also known as Version of record

Link to publication in VU Research Portal

citation for published version (APA)
Leever, K. A., Gabrielsen, R. H., Sokoutis, D., & Willingshofer, E. (2011). The effect of convergence angle on the kinematic evolution of strain partitioning in transpressional brittle wedges: Insight from analog modeling and high-resoluiton digital image analysis. *Tectonics*, [30]. https://doi.org/10.1029/2010TC002823

The effect of convergence angle on the kinematic evolution of strain partitioning in transpressional brittle wedges: Insight from analog modeling and high-resolution digital image analysis

Karen A. Leever,[1,2] Roy H. Gabrielsen,[1] Dimitrios Sokoutis,[3] and Ernst Willingshofer[3]

[1] Using analog modeling aided by digital image analysis (DPIV), we constrained the long-term kinematic evolution of strain partitioning in transpressional brittle wedges as a function of convergence angle. We ran a series of dry quartz sand experiments representing highly oblique continent-continent collision (convergence angles of 4° to 30°). The digital image analysis provided high-resolution constraints on the long-term kinematic evolution of these wedges, which could be subdivided in distinct kinematic stages, comprising (1) an initial "distributed strain" stage and (2) an "oblique wedge" stage before (3) the stage of strain partitioning is reached. Thus, we document the evolution of different deformation stages from a single plate tectonic boundary condition. In addition, the relationship between convergence angle, kinematic stages, and wedge geometry (including fault dips and fault hierarchy) was established. The modeling results show that smaller convergence angles lead to steeper faults. Besides, for a constant convergence angle, the proshears that evolved during the strain partitioning stage were less steep than those formed during the oblique wedge stage. The fault slip vector on individual fault segments was derived from the DPIV data set for each time increment, quantifying the magnitude and orientation of slip on fault segments during the different kinematic stages. In addition, in the 7.5° and 15° models, rotation of the slip vector by up to 40° was observed on a single proshear during the strain partitioning stage. These observations allow to some degree a validation of existing analytical models of strain partitioning, in particular the assumption of steady state.

1. Introduction

[2] In transpressive tectonic settings, strain partitioning between a fault system accommodating displacement parallel, and faults and folds formed in response to a component more orthogonal to the plate boundary is commonly observed, both in continent-continent and in oblique subduction systems (Figure 1). Some examples are the West Spitsbergen fold and thrust belt [*Lowell*, 1972; *Maher and Craddock*, 1988], the San Andreas fault system [e.g., *Jones and Tanner*, 1995; *Titus et al.*, 2007], the Palmyrides in Lebanon [*Weinberger et al.*, 2009], Trinidad [*Jamison*, 1991], Ryukyu/Taiwan [*Lallemand et al.*, 1999], New Zealand [*Koons and Henderson*, 1995; *Upton et al.*, 2003], Sumatra [*Yu et al.*, 1993] and southern Chile [*Polonia et al.*,

2007]. Along obliquely convergent subduction margins, an alternative manifestation of strain partitioning is back-arc spreading, which may cause a difference between the plate motion vector and the slip vector derived from earthquake fault plane solutions [*Yu et al.*, 1993]. In the present contribution, we focus on transpression and strain partitioning in brittle wedges, representing highly oblique continental collision at different convergence angles. Convergence angle α is defined as the angle between the plate motion vector and the plate boundary, where $\alpha = 90°$ represents orthogonal convergence and $\alpha = 0°$ strike slip. An alternative way to express the plate kinematics is in terms of (convergence) obliquity, representing the angle between the plate vector and the normal to the plate boundary.

[3] A first quantitative kinematic description of transpressive strain was given by *Sanderson and Marchini* [1984], who considered it "as a wrench or transcurrent shear accompanied by horizontal shortening across, and vertical lengthening along the shear plane." The model in this and further kinematic studies [*Fossen and Tikoff*, 1993; *Tikoff and Fossen*, 1993; *Tikoff and Teyssier*, 1994] consisted of a vertical zone of distributed deformation, with a discrete fault in

---

[1]Department of Geosciences, University of Oslo, Oslo, Norway.
[2]Now at Department of Lithosphere Dynamics, Deutsches GeoForschungsZentrum, Potsdam, Germany.
[3]Faculty of Earth- and Life Sciences, VU University of Amsterdam, Amsterdam, Netherlands.
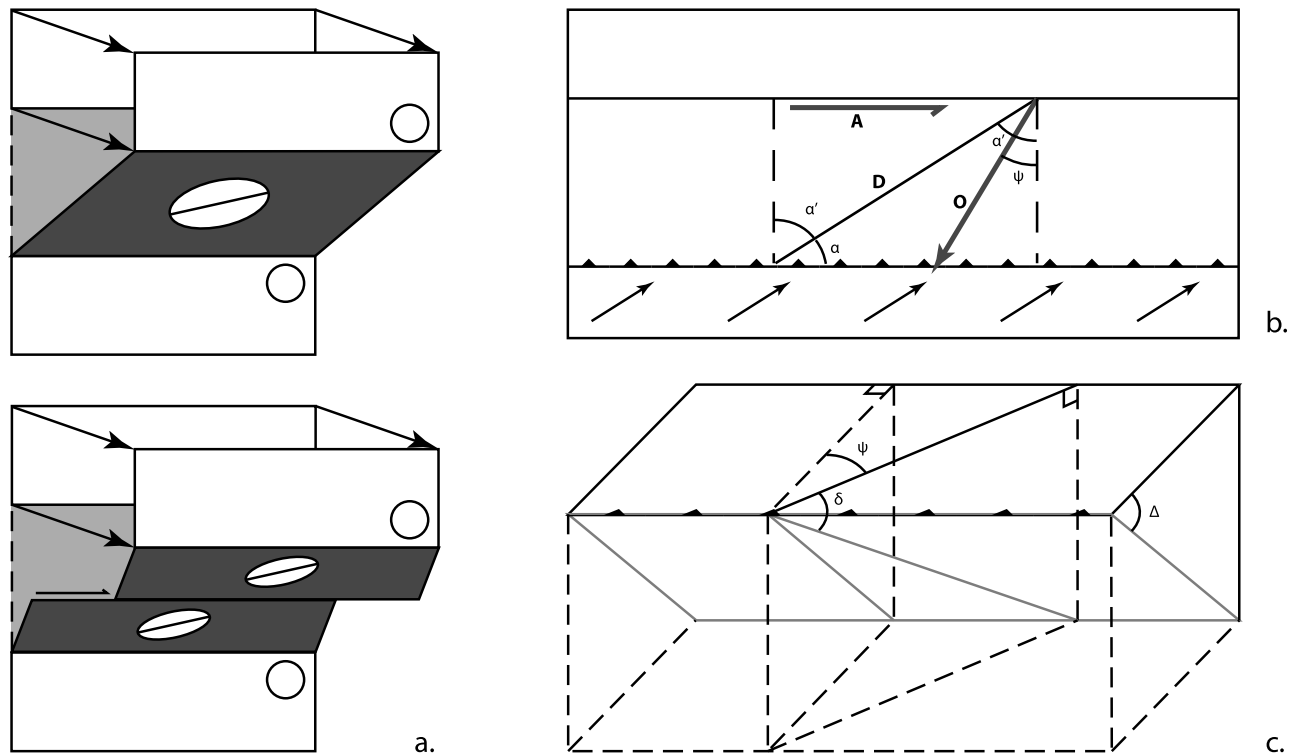
Figure 1. (a) Transpression without and with strain partitioning (modified from *Tikoff and Teyssier* [1994], with permission from Elsevier). (b, c) Oblique convergence **D** at an angle α to the plate boundary is partitioned into along-strike displacement **A** on a vertical fault at the back and slip at a higher angle to the plate boundary **O** on an inclined fault plane at the front.

the center if strain partitioning was assumed in addition (Figure 1a). Transpressional deformation and strain partitioning have been further studied (analytically) in terms of mechanics [*Haq and Davis*, 2010; *McCaffrey*, 1992; *Platt*, 1993, and references therein], and by means of analog [e.g., *Burbidge and Braun*, 1998; *Casas et al.*, 2001; *Del Castello et al.*, 2005; *Haq and Davis*, 2010; *McClay et al.*, 2004; *Pinet and Cobbold*, 1992; *Richard and Cobbold*, 1990; *Scheurs and Colletta*, 1998] and numerical models [*Braun and Beaumont*, 1995; *Koons*, 1994; *Upton et al.*, 2003; *Vernant and Chéry*, 2006]. These models consider either oblique subduction or continent-continent convergence. The corresponding geometry of the partitioned systems is that of a wedge bounded at the base by a horizontal or inclined surface accommodating slip at a high angle to the plate boundary, and at the back by a vertical strike-slip fault (Figures 1b and 1c).

[4] These authors have first of all attributed the *occurrence* of strain partitioning at oblique plate boundaries to convergence angle (α) and/or to rheology. From early experiments it was concluded that a ductile lower crust would be required [*Richard and Cobbold*, 1990]. Other studies have since shown that strain partitioning also develops for a brittle rheology after sufficiently large displacement [e.g., *Burbidge and Braun*, 1998]. Based on numerical and analog experiments as well as analytical modeling, the critical convergence angle for strain partitioning to occur was derived to be around 25°–30° for a brittle rheology, whereas it will theoretically not evolve for lower obliquities [*Braun and Beaumont*, 1995; *Burbidge and Braun*, 1998; *Haq and Davis*, 2010]. Still, strain partitioning has been observed at

margins with higher plate convergence angles, such as Sumatra where the plate convergence angle is 50° [*Yu et al.*, 1993].

[5] Besides, the *degree* of strain partitioning has been a subject of investigation, i.e., which fraction of the margin parallel displacement is accommodated "on a nearly vertical fault located on the continental side of a zone of plate consumption" [*Fitch*, 1972; *Fossen and Tikoff*, 1993]. It has been observed and modeled that transpressional strain is generally not fully partitioned between pure strike slip and pure convergence. Instead, the slip vector (ψ) derived from earthquake focal mechanisms lies between the plate motion vector α and the margin perpendicular [e.g., *McCaffrey*, 1992; *Teyssier et al.*, 1995; *Yu et al.*, 1993] (Figure 1b). From analytical models of brittle transpressional wedges it was concluded that ψ is constant and a function of the angle of internal friction φ and, in case of an inclined lower slip surface, its dip Δ [*Burbidge and Braun*, 1998; *Haq and Davis*, 2010; *McCaffrey*, 1992] (Figures 1b and 1c).

[6] The existing analytical solutions assume steady state conditions. However, it has been noted that a minimum amount of strain is required for strain partitioning to evolve: it does not occur until a strike-slip fault has formed in the center of the transpressional wedge [*Burbidge and Braun*, 1998]. Until this stage of development, the wedge kinematics is necessarily different. This long-term kinematic evolution of transpressional wedges, as a function of convergence angle, has not yet been documented in any detail in previous experimental work. This is mostly because the experiments were run for low total displacement, or because
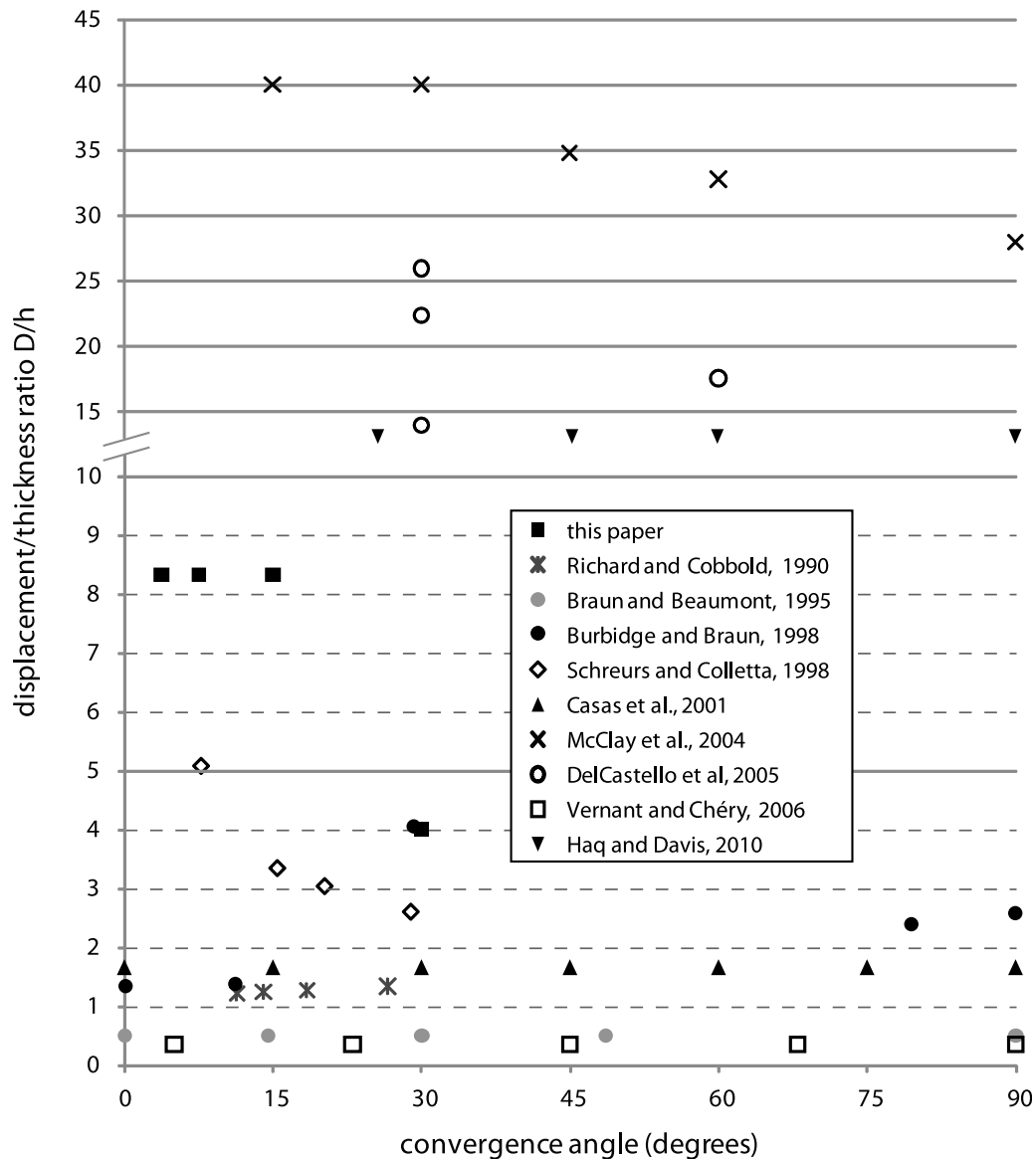
Figure 2. Ratio of total displacement to model thickness (D/h) versus convergence angle in the present study and in previous experimental work. Note scale change of vertical axis at 10. Numerical models by *Vernant and Chéry* [2006] and *Braun and Beaumont* [1995]; the others are crustal or basin-scale analog modeling studies. Note that most of the previous experiments are restricted to low total strain (D/h < 3), while some feature extremely large deformation with ratios up to 40. The present experiments were conducted for intermediate total strain. In this domain the changes between kinematic stages were found to occur.

the authors rather focused on the final stage geometry (Figure 2).

[7] To fill this gap, we used analog tectonic modeling combined with digital image analysis. This yielded high-resolution constraints on the long-term kinematic evolution of transpressional brittle wedges, including the occurrence (initiation, expression) and degree of strain partitioning as a function of convergence angle. We discuss how these new and detailed constraints on the kinematics of even individual fault segments allow validation of existing analytical mechanical models, in particular the assumption of steady state. In the companion paper [*Leever et al.*, 2011], the

detailed definition of model kinematic stages that this new method provides is applied to the Tertiary West Spitsbergen fold and thrust belt through comparison with field kinematic data.

2. Modeling Strategy and Setup

[8] A series of experiments with brittle rheology was run at the Tectonic laboratory at the VU University in Amsterdam (Teclab) to study the progressive kinematic evolution of transpressive deformation in response to a constant plate tectonic boundary condition. We used quartz sand to build brittle models which were deformed at different convergence

Table 1. Model Setup[a]

Model ID	Angle (deg)	Displacement D (cm)			v (cm/h)	h (cm)	D/h[b]
		Total	dx	dy			
wsftb32	4	50	3.3	49.9	12	6	8.3
wsftb33	7.5	50	6.5	49.6	12	6	8.3
wsftb34	*15*	*50*	*12.9*	*48.3*	*12*	*6*	*8.3*
wsftb38	30	24	12.0	20.8	12	6	4.0

[a]Italic font indicates reference model. Here dx and dy are components of total displacement orthogonal and parallel to velocity discontinuity, respectively.

[b]See also Figures 2 and 7.

angles and with a total displacement **D** ≫ thickness of the sand pack **h** (Figure 2 and Table 1). In addition to visual inspection during the model runs, progressive deformation was monitored with digital photography from the top. From these pictures, an incremental velocity field was calculated

for each time step using digital particle image velocimetry (DPIV). At the end of the model run, the sand pack was carefully covered with loose sand to protect the topography. It was then saturated with water and cross sections were sliced perpendicular to the plate boundary at 5 cm spacing.

2.1. Model Setup: Geometry and Kinematic Boundary Conditions

[9] The model setup is shown in Figure 3. Two 1 mm thick, low friction plastic sheets were placed on a flat base at a relative angle α which was varied between 4 and 30 degrees. The upper sheet was fixed to the table top while the lower sheet was mobile and attached by means of flexible straps to an engine which pulled at a constant rate. Model parameters such as convergence angle and displacement are shown in Table 1. A sand pack of 6 cm thickness and with an extent of 120 × 70 cm consisting of quartz sand was sieved onto the basal plastic sheets (Figure 3b). The model thus has a
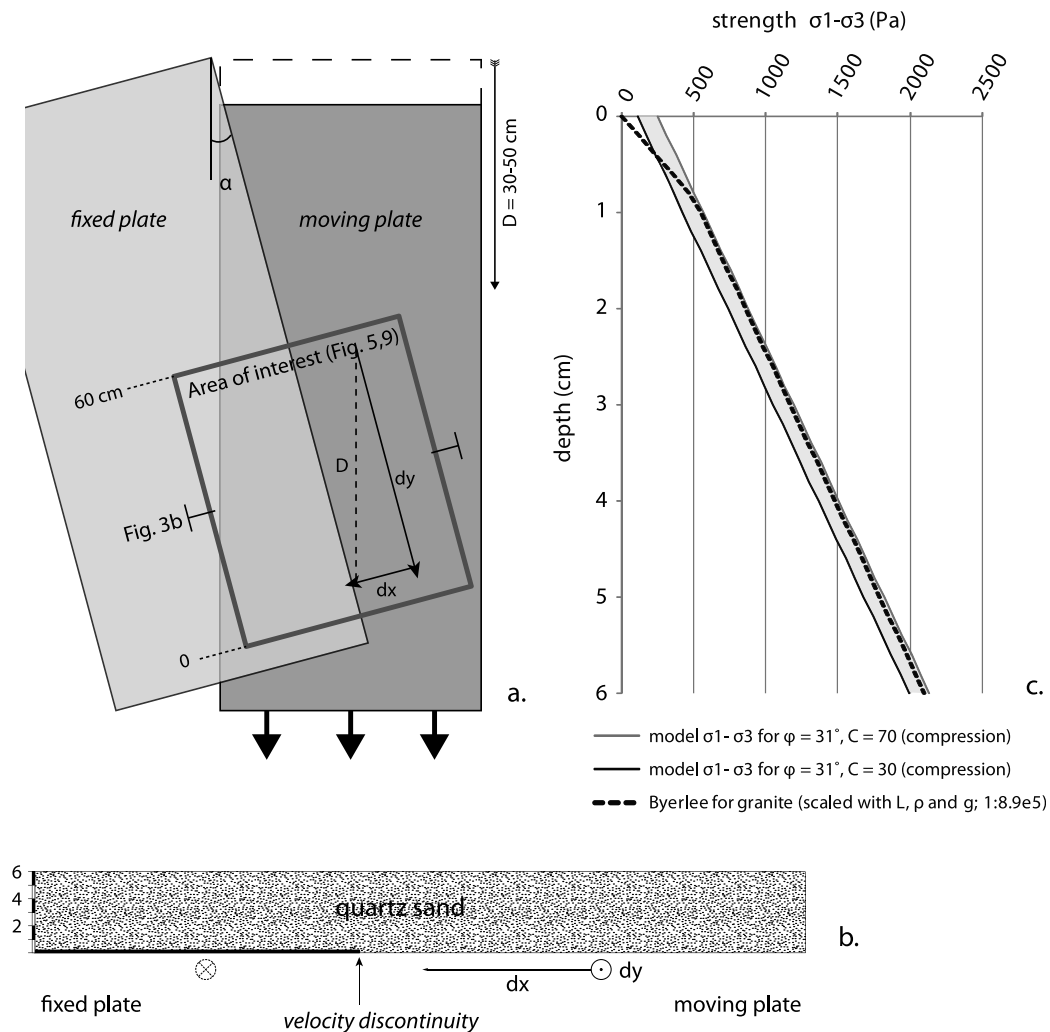
Figure 3. Modeling setup. (a) Top view. D is total displacement of the lower plate, and dy and dx are corresponding components along-strike and orthogonal to the edge of the fixed upper plate or velocity discontinuity. (b) Cross section perpendicular to the basal velocity discontinuity. See Table 1 for values of dx and dy. (c) Yield strength envelope for quartz sand and scaled natural prototype, granite.

very simple setup with a constant kinematic boundary condition and a homogeneous brittle rheology.

[10] The long edge of the stationary upper basal sheet (Figure 3a) formed a velocity discontinuity, similar to the "S point" or "strain rate singularity" as defined in 2D by *Willett et al.* [1993] and *Beaumont et al.* [1994]. The model setup is intrinsically asymmetric, leading to advection of material from the proside (overlying the moving basal plate) toward the retroside (above the stationary plate) of the model. This is similar to the model setup used in a number of analog studies of obliquely convergent margins [e.g., *Burbidge and Braun*, 1998; *Casas et al.*, 2001; *McClay et al.*, 2004] but different from *Richard and Cobbold* [1990], who used a symmetrical basal kinematic boundary condition.

2.2. Model Scaling and Rheology

[11] In scaled experiments, quartz sand is commonly used as a physical analog to brittle (upper crustal) rocks. This has been done in a large number of tectonic analog modeling studies obeying the scaling rules of dynamic similarity [*Hubbert*, 1937]: if a scaled model is to be representative of its counterpart in nature, similar distributions of stresses, rheologies and densities are required.

[12] The sieved quartz sand we used has a grain size of 300 μm, a density of 1510 kg/m^3, cohesion of 30–70 Pa and an angle of internal friction of 31°. The length scaling in our model is 1:500,000 or 2×10^{-6}; that is, 1 cm in the model corresponds to 5 km in nature. The ratio of the densities of model (quartz sand) and prototype (granite, 2700 kg/m^3) is approximately 1.6, resulting in a scaling factor of 1.25×10^{-6} for the stresses or brittle strength. Note that for the current length scaling, the total thickness of the brittle layer corresponds to 30 km, which we acknowledge is rather large.

[13] The stress "distributions" mentioned above are best imaged by a yield strength envelope (YSE) [*Goetze and Evans*, 1979; see also *Ranalli*, 1997; *Burov*, 2007] (Figure 3c). The construction of the brittle YSE is based on the Mohr-Coulomb failure criterion, rewritten in terms of differential stress [*Kirby*, 1983; *Schellart*, 2000; *Sibson*, 1974]. The compressional brittle strength ($\sigma_1 - \sigma_3$) of the model quartz sand is shown in Figure 3c for the parameters given above. There is a good agreement with the strength of granite according to *Byerlee* [1978], scaled by the factor of 1.25×10^{-6}. See the appendix of the companion paper [*Leever et al.*, 2011] for more details.

3. Digital Image Analysis

[14] In some previous laboratory studies of transpressional wedges and strain partitioning, kinematics and strain were derived from a displacement field that was calculated from the displacement of passive markers on the model surface [*Haq and Davis*, 2010, 2009; *Koons and Henderson*, 1995; *Pinet and Cobbold*, 1992]. The resolution of the displacement field obtained this way depends on the spacing of the markers and is generally poor; sufficient to calculate bulk strain in a segment of the wedge but not good enough to resolve slip on individual closely spaced fault segments [see, e.g., *Haq and Davis*, 2010]. To avoid such problems, we used the particle tracking method digital particle image

velocimetry [*Westerweel*, 1993]. This method has the advantage of a much higher resolution, basically depending on the resolution of the camera and the displacement interval between two subsequent pictures. See also *Adam et al.* [2005] for a more general application in analog tectonic modeling.

3.1. DPIV Recording

[15] The experiment surface was sprinkled with low-density marker particles to enhance the quality of correlation (C. Schrank, personal communication, 2008). The camera was suspended above the model and consistently positioned such that the long side of the image was parallel to the basal velocity discontinuity, resulting in a grid optimally oriented for subsequent analysis. The DPIV method was used to analyze photos of the model surface, which were taken at regular intervals during progressive deformation. It uses pattern recognition to calculate a velocity field of incremental deformation from two subsequent images (Figure 4a). We used the open source software MatPIV [*Sveen*, 2004] for Matlab® with some modifications in the postprocessing routines. For the available camera resolution and the image field of view, we obtained a vector field consisting of about six displacement vectors per square centimeter.

3.2. Surface Expression of Fault Kinematics and Fault Slip Analysis

[16] For analysis and visualization of fault kinematics (e.g., Figures 6 and 11), a directional derivative **dv** of the original velocity field was calculated by simply subtracting adjacent vectors in the x direction (Figure 4). Mathematically, the operation can be expressed by

$$\mathbf{dv} = \mathbf{v}(\mathrm{x}, \mathrm{y}) - \mathbf{v}(\mathrm{x} + 1, \ \mathrm{y})$$

where **v** is the initial vector field and **dv** its directional derivative.

[17] Fault slip was calculated instead of strain, because it gives a better impression of strain partitioning, displaying the relative movement of fault blocks by highlighting the deformation zones between them. Within the (semi-) rigid fault blocks, the displacement field is constant and subtraction of adjacent vectors gives a resultant ≈ 0. Across a fault, the magnitude and orientation of the vector field changes and the differential vector $\neq 0$ (Figures 4b and 4c). In case the length of one of the vectors in **dv** exceeded a threshold value, its azimuth (0°–360°) was plotted according to a color scale (Figure 4d). Thus, on faults aligned in the y direction, red shades consistently indicate convergence and purple shades dextral strike slip. Calculating a directional derivative in the x direction implies that changes in the y direction are not taken into account. The method is therefore best suited for the derivation of fault kinematics along fault segments elongated in the y direction, which is generally the case for our model.

[18] In a next step, the fault slip evolution on individual fault segments was quantified (Figures 4f and 4g). The analysis was based on the fault kinematics diagrams. Windows with a width of 10 cm were defined in the center of the models, away from possible boundary effects. A
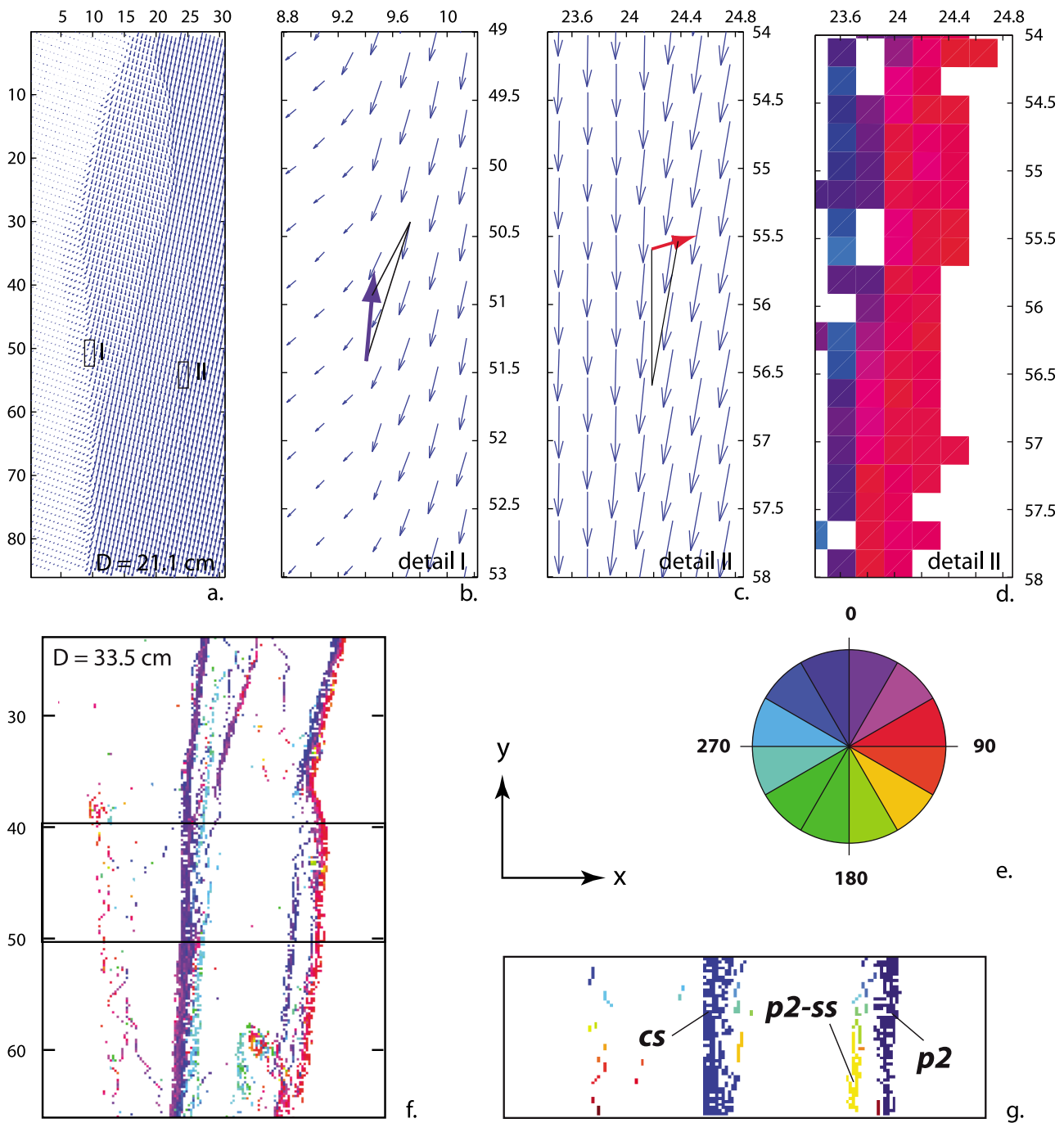
Figure 4. Derivation of fault kinematics. (a) DPIV output, vector field of incremental displacement after 21.1 cm of displacement of the lower plate. (b, c) Subtraction of adjacent vectors in the x direction consistently yields an azimuth around 0° for dextral strike slip and 90° for contraction on faults that strike N–S. (d) Color coding according to azimuth if the size of the resultant vector exceeds a threshold value. (e) Color scale for fault slip azimuth (Figures 4d and 4f). On faults striking N–S, red colors consistently indicate reverse faulting, dark blue to purple means dextral strike slip, light blue means extension, and green means sinistral strike slip. (f) Fault kinematics plot for D = 33.5 cm showing search window for fault slip analysis. (g) Automatically color coded pixel clusters within search window. These color-coded pixel clusters were classified by manually identifying the fault segment they represent. Fault slip was calculated for each identified fault segment (see Figures 12 and 13).

Table 2. Main Structures in the Model Transpressional Belts[a]

	Description
R	Riedel shears [*Riedel*, 1929]. Only in 4° model
p	Proshears p0–p3. Transient faults with a vergence toward the down going basement plate, accommodating part of the orthogonal component of the imposed displacement field. Strike (sub) parallel to the basal velocity discontinuity. Dip of 30–55 degrees. Both dip and fault spacing are greater for smaller convergence angles. Oblique to reverse slip.
r	Retroshear. Long-lived fault with a vergence toward the stationary (upper) basement plate, accommodating part of the orthogonal component of the imposed displacement field. Strike (sub) parallel to the basal velocity discontinuity. Dip of 35°–55° (larger for smaller convergence angles). Oblique to reverse slip.
rs	Strike-slip fault branching from retroshear. Subvertical, strikes (sub) parallel to the basal velocity discontinuity.
ls	Linking shear zone. Steep strike-slip fault striking parallel to displacement direction, merging with *p* and *r* on the sides. Not developed in 4° model.
cs	Central shear zone (Y shear). Major subvertical strike-slip fault, (sub) parallel to and overlying the basal velocity discontinuity.

[a]We use lowercase letters to refer to the structures in our models instead of capitals to avoid confusion with well-established terminology in strike-slip settings (Riedel and P shears).

routine in Matlab® was used to label clusters of pixels corresponding to segments of the main faults and extract the information about the fault slip vector **dv** contained in them. A weighted average value of the fault slip vector was calculated for those pixel clusters (n > 10). The labeled clusters were subsequently classified through manual identification (Figures 4f and 4g).

4. Results

[19] To facilitate the description of the variance of the experiments, the model with an intermediate convergence angle (15°), which moreover produced the clearest expression of strain partitioning, was selected as a reference. In the following, this reference model is described in detail, thereby introducing the nomenclature for the most important structural elements (Table 2). The DPIV method allowed easier recognition of active faults and changes in kinematics. These were used to define different stages in the kinematic evolution, which are again outlined first for the reference model. Subsequently, the geometry and kinematics (including fault slip on individual segments) of the other models are described, focusing on the effect of convergence angle on the kinematic evolution of a transpressional wedge. For convenience, a reference frame is defined in which the basal velocity discontinuity strikes north-south with the moving lower basement plate to the east. The top of the (map view) images is thus to the north.

4.1. Reference Model: The 15° Convergence Angle

4.1.1. Geometry

[20] The interpretation of the reference experiment fault patterns in top view at the end of the model run (Figure 5a) was aided by studying the model kinematic evolution
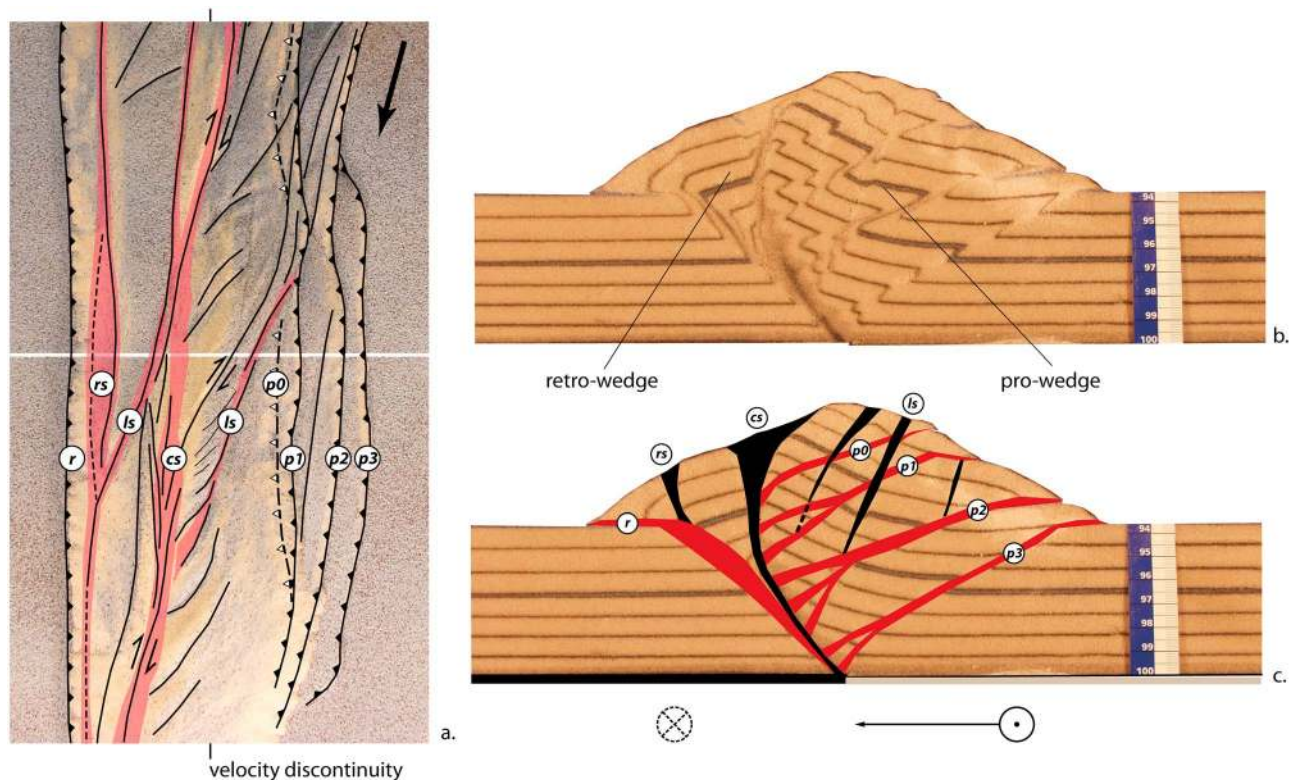
Figure 5. Geometry of 15° reference model. (a) Top view, (b) uninterpreted cross section, and (c) interpreted cross section. Red color is used for faults accommodating significant orthogonal displacement in addition to strike slip.
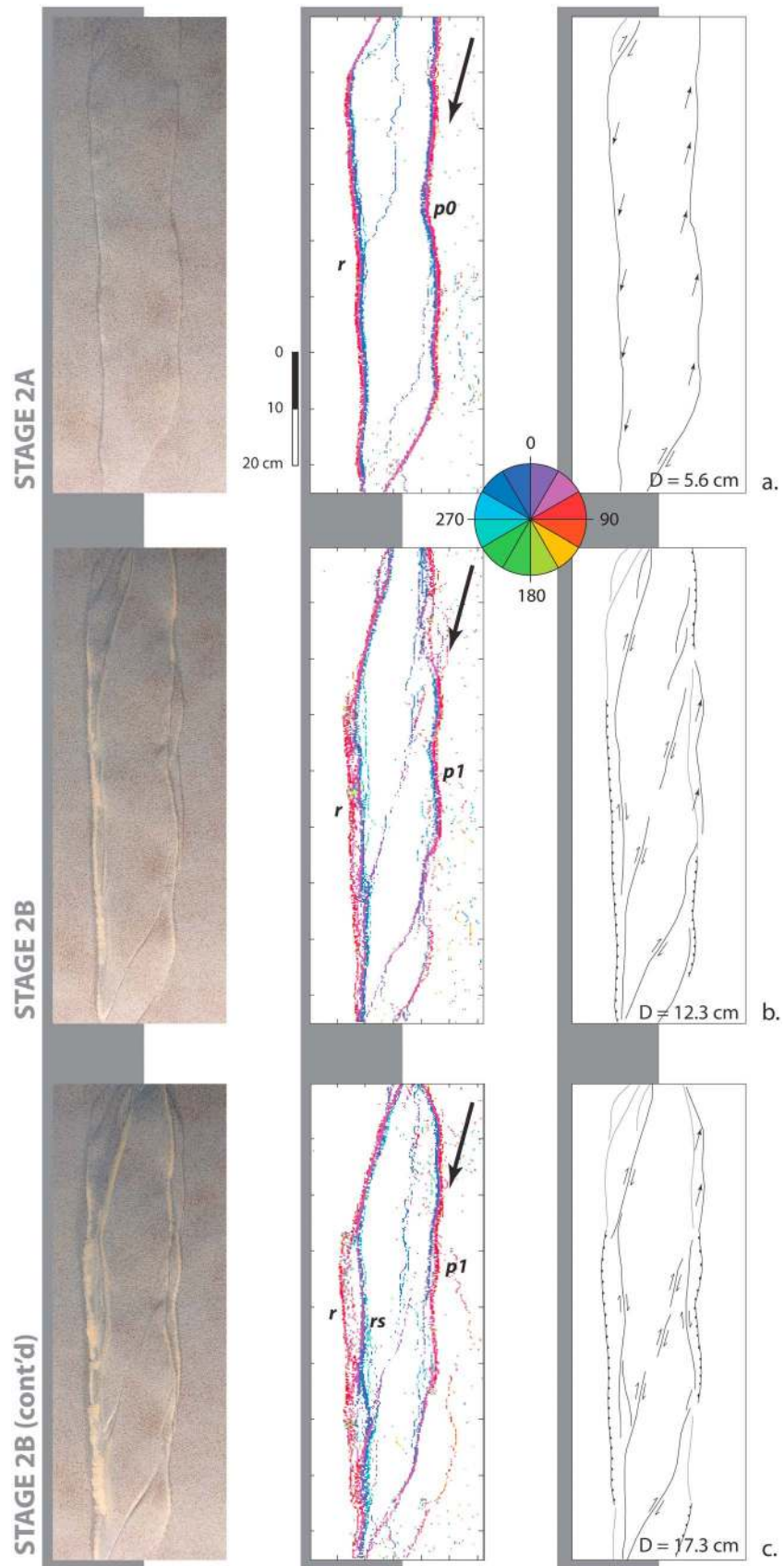
Figure 6

(Figure 6) and cross sections. The most important structures are the retroshear (*r*), the central shear zone (*cs*) and proshears (*p0–p3*) (Figure 5a and Table 2). In addition, the major strike-slip faults *rs* and *ls* are highlighted; *ls* representing the linking shear zone (which was later offset by displacement along the *cs*; see section on kinematics), and *rs* the strike-slip fault associated with the retroshear *r*. *r*, *rs*, *cs* and the proshears are generally parallel to the basal velocity discontinuity while *ls* makes an angle of ~20° to it.

[21] In cross section (Figures 5b and 5c) the difference between these faults is more obvious. It shows an asymmetric wedge centered above the basal velocity discontinuity. A prowedge and retrowedge are separated by the central shear zone *cs*. *r* is the lower boundary of the retrowedge which shows only little internal deformation, while the prowedge is internally dissected by the closely spaced stacked proshears.

[22] The retroshear *r* with its strike-slip branch *rs*, and the central shear zone *cs* represent major, long−lived faults (see Figures 6 and 7a) along which material was advected upward. Both accommodated significant and rather similar uplift (note position of marker layer in Figure 5c). The retroshear *r*, *rs* and *cs* steepen and merge at depth. Until the activity on *r* and *rs* ceased, the joined lower part of these faults must have accommodated the displacement by oblique slip, which became progressively more partitioned toward the surface.

[23] On the proside, the space problem resulting from the advection of material upward along the retroshear was solved by displacement along a series of proshears. At depth, where they root on the retroshear or *cs*, two to three narrowly spaced faults merge into a single proshear toward the surface (Figures 5b and 5c). In addition to the proshears which have pronounced contractional components, the prowedge is dissected by strike-slip faults. The most important of these is the linking shear zone *ls*. This fault does not extend further downward than *p2*: it became extinct during the lifetime of *p2* (see also Figure 7a), and from then on the main strike-slip displacement was further accommodated by the *cs*.

[24] There is a clear difference in dip between the different types of faults (Figures 5 and 8). The proshears are all inclined at a shallow angle. The last formed proshear *p3* has a dip of ~30° while the older, abandoned and passively uplifted proshears show dips down to 20°. In contrast, the retroshear *r* has a dip of some 45°. The strike-slip faults are even steeper with angles of 70° (*rs*, *ls*) to 90° (*cs*).

4.1.2. Kinematics

[25] The DPIV method greatly facilitated the observation of the kinematic evolution of the models. We defined three different stages in the temporal and spatial evolution of the reference model, based on the active faults and the slip they accommodate. These are the (1) distributed strain stage, (2) shear lens stage and (3) strain partitioning stage (Figure 6).

The stages and their substages are described in more detail below.

[26] 1. In stage 1, the distributed strain stage (0 < D/h < 0.5), displacement was distributed over a wide area of the model surface centered above the basal velocity discontinuity. Faults, which had presumably already initiated at depth, were not yet observed at the surface. The width of the zone of distributed deformation reflects the width of the future shear lens (see Figure 11).

[27] 2. In stage 2, the oblique wedge stage (0.5 < D/h < 3.2), localization of displacement along two elongated shear zones parallel to the basal velocity discontinuity (*r* on the retroside and *p0* on the proside) became evident at the model surface in this stage (Figures 6a–6c). The faults accommodate oblique displacement and form the boundaries of an uplifting wedge. Two substages could be defined based on the local occurrence of strain partitioning on the bounding faults. These are (2a) without strain partitioning and (2b) with local strain partitioning on proside and retroside of the wedge.

[28] 3. In stage 2a (0.5 < D/h < 1.5; Figure 6a), the surface expression of the bounding faults was initially similar on proside (*p0*) and retroside (*r*); narrow fault zones accommodate oblique displacement.

[29] 4. In stage 2b (1.5 < D/h < 3.2; Figure 6b), the shear zone on the retroside split into two initially closely spaced branches, accommodating strike-slip displacement on the inner branch *rs* and reverse displacement on the branch *r* at the outside of the wedge. On the proside, though the shape of *p0* became more irregular, it still accommodated oblique slip. Some minor strike-slip faults crossed the center of the wedge, their small displacements expressed rather on the kinematics plots than on the photograph. Hence, strain was locally partitioned on the retroside of the model, while oblique faulting still characterized the proshear. With additional displacement (Figure 6c), the spacing between the inner strike-slip fault (*rs*) and the outer reverse fault on the retroside increased. Also on the proside, an inner branch accommodating along-strike displacement was separated from an outer branch accommodating reverse displacement, although the spacing between the two was small. Minor strike-slip faults subparallel to the bulk transport direction were still observed in the middle of the wedge.

[30] 5. In stage 3, the strain partitioning stage (D/h > 3.2) (Figures 6d–6f), displacement was partitioned between strike slip along one of the faults (*ls* or *cs*) crosscutting the uplifted basement wedge and (near) orthogonal displacement along the bounding proshears and retroshears.

[31] 6. In stage 3a (3.2 < D/h < 4.5; Figure 6d), a branch crosscutting the uplifted basement wedge formed, linking the strike-slip faults on proside and retroside that were formed in stage 2. This new "linking shear zone" *ls* made an angle of ~20 degrees to the basal velocity discontinuity and thus was (sub) parallel to the imposed displacement field, as

Figure 6. Fault kinematics for 15° reference model showing expression of (a–c) stage 2 and (d–f) stage 3. (left) Picture (top view), (middle) fault kinematics from PIV analysis, and (right): interpretation of active (black) and abandoned (gray) faults. Faults accommodating predominantly reverse slip are adorned with pointed teeth, and arrows and arrow pairs indicate oblique slip and strike slip, respectively. Gray shading in background indicates position of upper stationary plate; black arrows in Figure 6 (middle) point in displacement direction of lower plate. The star in Figure 6d indicates the future position of the *cs*.
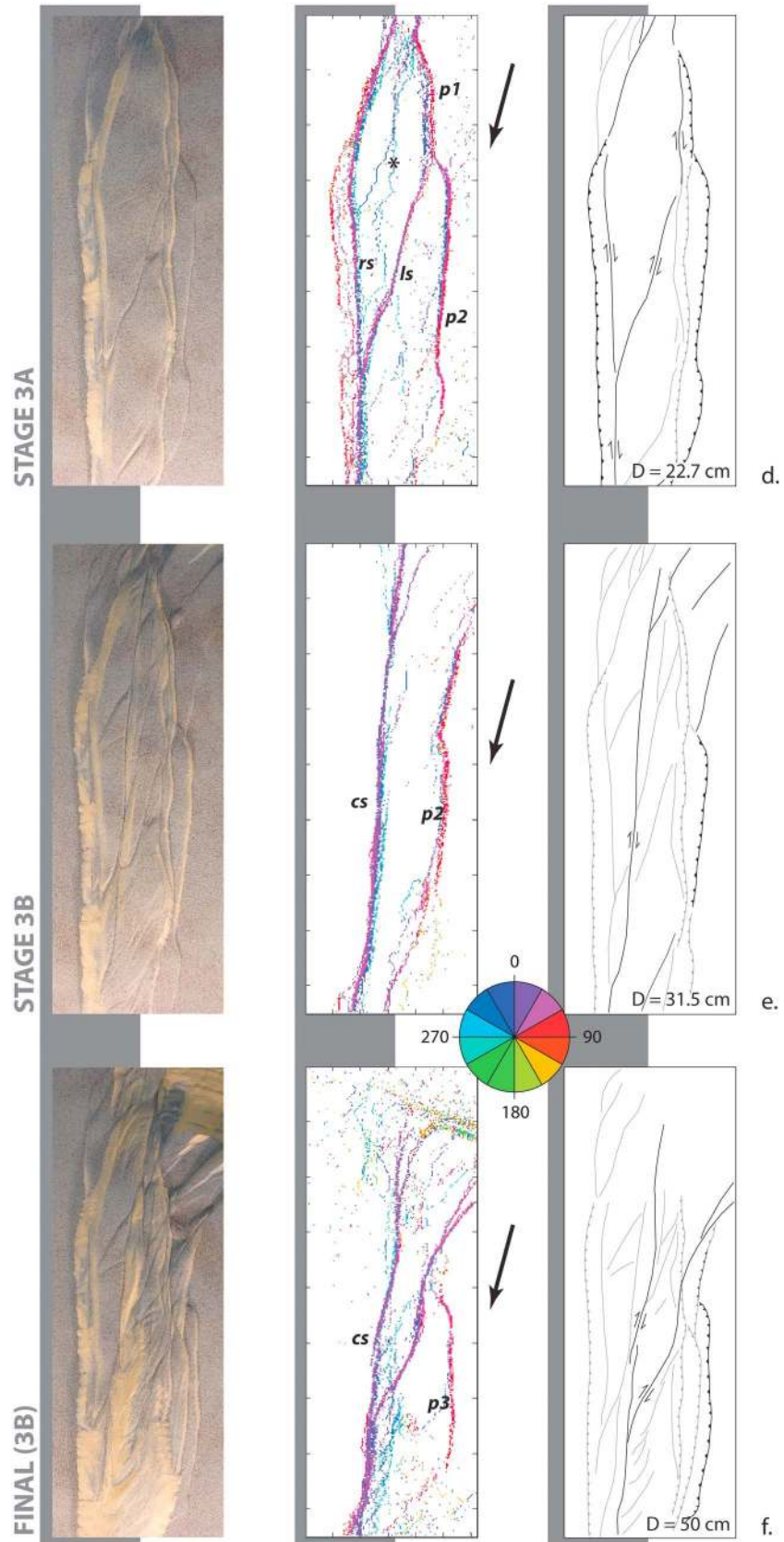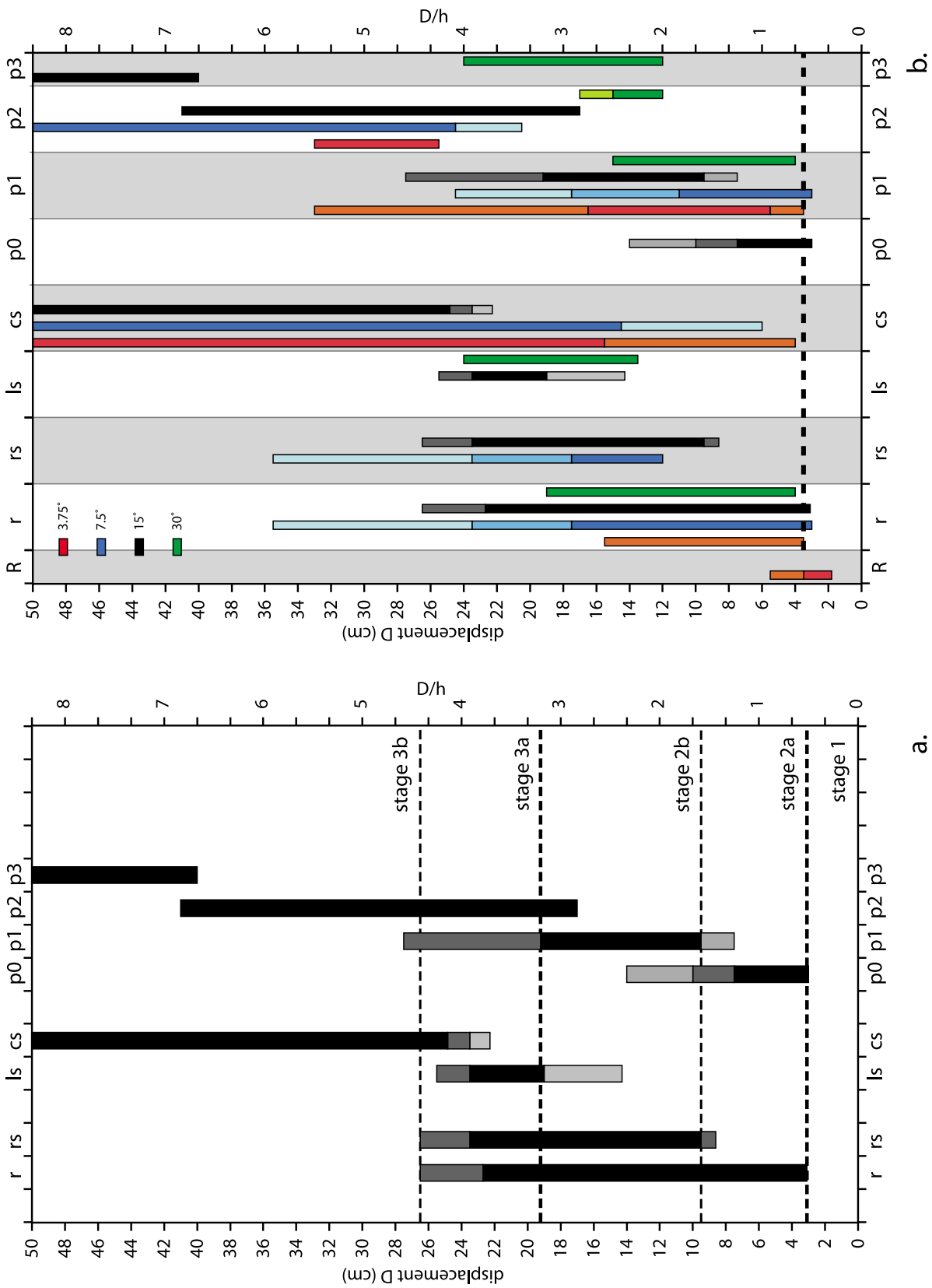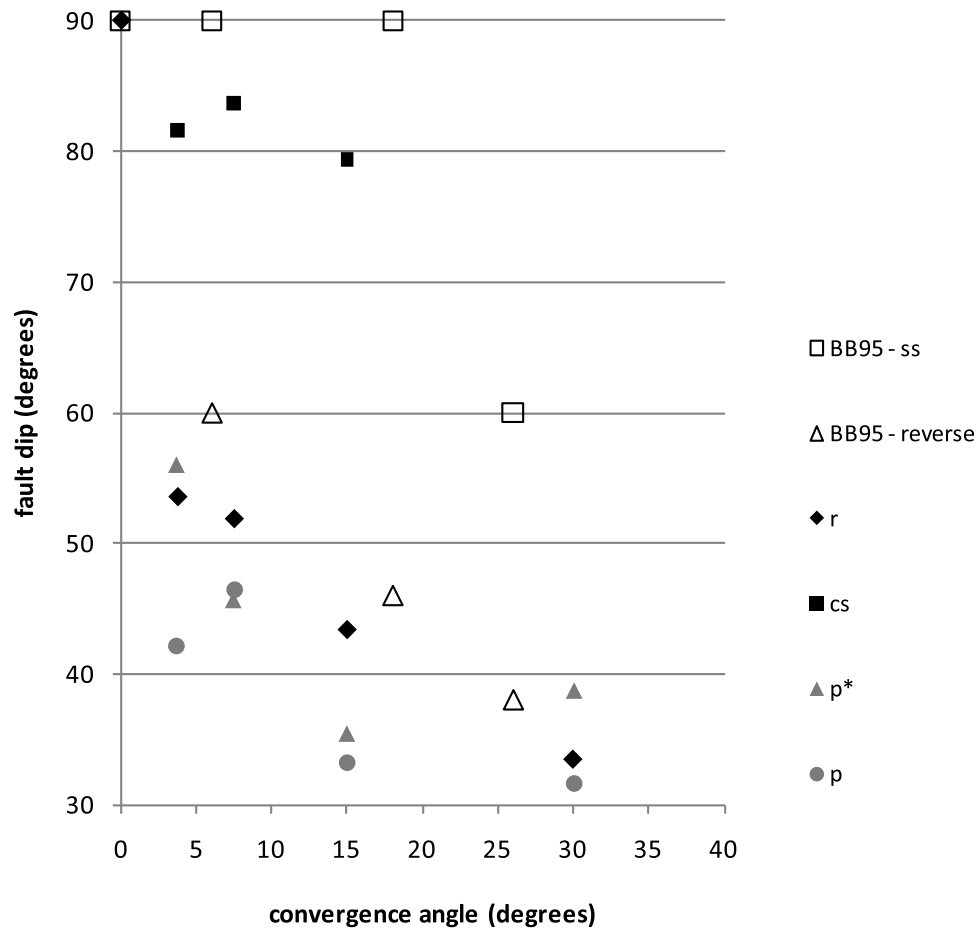
Figure 6. (continued)

Figure 7. (a) Kinematic stages and active structures for the 15° reference model. The *x* axis, active structures (see Figure 6); the *y* axis, cumulative displacement and D/h. Dark shades indicate fully active structure, and lighter shades mean that activity is decreasing or building up. (b) Active structures for all models. Light/dark shading as in Figure 7a.

Figure 8. Fault dips as a function of convergence angle for *r*, *cs*, the most external proshear *p*, and the one on the inside of it, *p**. For comparison, see the results of *Braun and Beaumont* [1995].

opposed to the preexisting strike-slip faults which were parallel to the basal velocity discontinuity. The appearance of the *ls* was just preceded by the formation of a new proshear (*p2*). The reverse fault *p2* and the strike-slip fault *ls* extended over the same (southern) part of the wedge. In this part of the wedge, displacement was partitioned between strike-slip displacement along *ls* and predominantly reverse displacement along *p2*. To the contrary, in the northern part of the wedge displacement was accommodated by (locally partitioned) oblique shear along *p1*. Part of the along-strike displacement was still accommodated by *rs* in addition to *ls*. In the course of this stage, *ls* and *rs* merged into a new shear zone subparallel to and above the basal velocity discontinuity, *cs*.

[32] 7. In stage 3b (D/h > 4.5; Figures 6e and 6f), all along the strike of the wedge, deformation on the retroside of the wedge ceased and strike-slip displacement was accommodated by the central shear zone. The *cs* accommodated major uplift in addition to the along-strike displacement. On the proside of the model, *p2* and finally *p3* accommodated orthogonal displacement.

[33] The correlation between the (duration of) the kinematic stages and the main active structures is summarized in Figure 7a. Obviously, no faults were recognized in the distributed strain stage (stage 1). Retroshear *r* and the first

proshear *p0* appeared simultaneously and this defined the start of stage 2a. The separation of the retroshear into a contractional (*r*) and a strike-slip (*rs*) branch coincided with the formation of a new proshear (*p1*) and defined the start of stage 2b. Stage 3a started when the linking shear zone *ls*, which had been developing for a while, became a pronounced structure. Note that during this stage most major structures were active (*p1* and *p2* on different segments of the wedge). The end of stage 3a was defined by the disappearance of *r* and *rs*. The central shear zone *cs* had become activated prior to that. In stage 3b strain was most completely partitioned between strike-slip movement along the *cs* and reverse displacement along the faults bounding the wedge on the (pro) side.

4.2. Effect of Convergence Angle

[34] In three additional model runs, the convergence angle was varied between 4, 7.5 and 30 degrees (Table 1). The effect of convergence angle on kinematics and final geometry is described below. Moreover, fault slip on individual fault segments was determined for the 4°, 7.5° and 15° models, allowing for quantification of the evolution of strain partitioning and its progressively changing degree. The latter is also expressed in the dip of the proshears that was calculated from fault spacing for the 7.5° and 15° models.
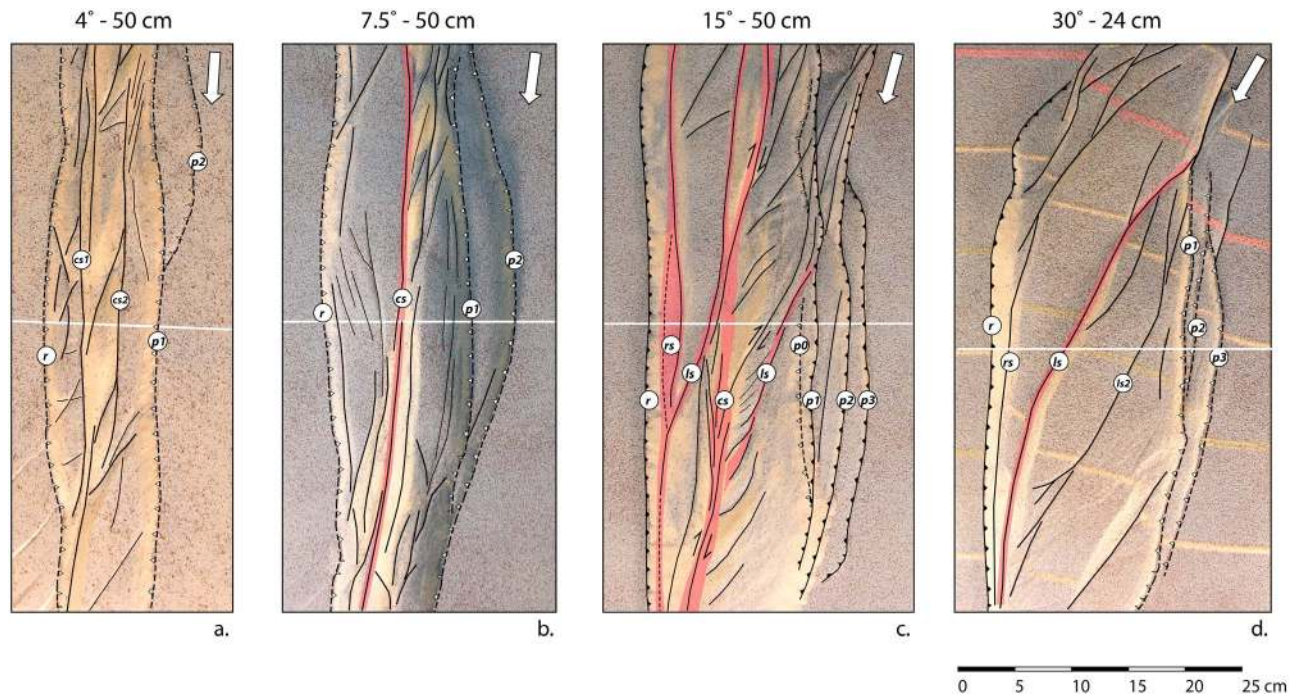
Figure 9. Effect of changing convergence angle on geometry. Top view for (a) 4°, (b) 7.5°, (c) 15°, and (d) 30° models. White lines indicate position of cross sections presented in Figure 10.

4.2.1. Geometry

[35] Several structural elements were common for all of the models, independent of the convergence angle (Figures 9 and 10). These are the retroshear r, central shear zone cs and proshears p. However, there are also marked differences between the models. These are expressed, e.g., by the width of the wedges, fault types and (relative) fault dips. Again, the interpretation of the fault patterns in top view was aided by studying the models' kinematic evolution and cross sections.

[36] The 4° model showed the narrowest deformation zone (~10 cm wide, and 13 cm where $p2$ is present) and relatively few major faults (Figure 9a). The wedge was bounded by retroshear r and proshear $p1$. A second proshear ($p2$) surfaced only in the northernmost part of the model. An oblique linking shear zone (ls) was not observed; in contrast, it has two well developed central shear zones (cs and $cs2$) parallel to the basal velocity discontinuity. The center of the belt shows remnants of an initial array of Riedel shears. In cross section (Figure 10a), the deformed wedge has the rather symmetrical shape of a flower structure with steep faults rooting on or near the basal velocity discontinuity. The faults are straight or convex-up, though concave-up geometries are also observed. The largest uplift is accommodated by $p1$ and the two cs faults, between which a narrow wedge is extruding nearly vertically.

[37] The 7.5° model features r, rs, cs and two proshears (Figure 9b). The faults are subparallel to the basal velocity discontinuity, except $p2$ which swings inward toward the southern edge of the model. The wedge has a maximum width of ~19 cm. In cross section (Figure 10b), the deformed wedge again looks rather symmetric; less than the 4° model but more so than the 15° model. The shape of the wedge still resembles a flower structure, except for $p2$ which branches on the cs at a near-orthogonal angle, similar to the proshears

in the reference model (Figure 10c). This difference in geometry between $p2$ and $p1$ is due to the change in kinematic evolution: $p2$ is active in the strain partitioning stage (see section 4.2.2). This model also features an extruded narrow wedge in the center of the model between cs and $p1$. The difference with the 4° model is in the dips of $cs2$ (in the 4° model; Figure 10a) and $p1$ (in the 7.5° model; Figure 10b). Due to its shallower dip, the latter accommodates shortening in addition to uplift. Uplift along the subvertical cs, in both cases, leads to collapse of the slope. Note that, in contrast, the original topographic surface is largely preserved in the hanging wall of $p1$. The uplift along a steep fault, leading to slope collapse, may involve rotation in addition to translation, while uplift along the less steeply inclined proshear leads to translation only and thus preservation of the topographic surface.

[38] The width of the wedge of the 30° model (Figure 9d) is largest of all models, even though this experiment was terminated after a smaller total displacement than the other models. In top view, it features a retroshear, ls and several closely spaced proshears. It shows the most pronounced structural asymmetry in cross section (Figure 10d). Albeit more narrowly spaced than in the 15° reference model, the proshears are also well developed. The number of proshears and their development, despite the smaller total displacement, are probably due to the larger component of orthogonal displacement for this model (Table 1).

[39] From the geometrical relationship between the faults in cross section (Figure 10), a fault hierarchy has been defined [see also *Bonini et al.*, 2000]. Faults are considered equivalent when branching from a common stem at similar dip angles, such as in a classical flower structure. A distinct hierarchical relationship is inferred where (subordinate) faults root at a high angle on another (master) fault. In terms
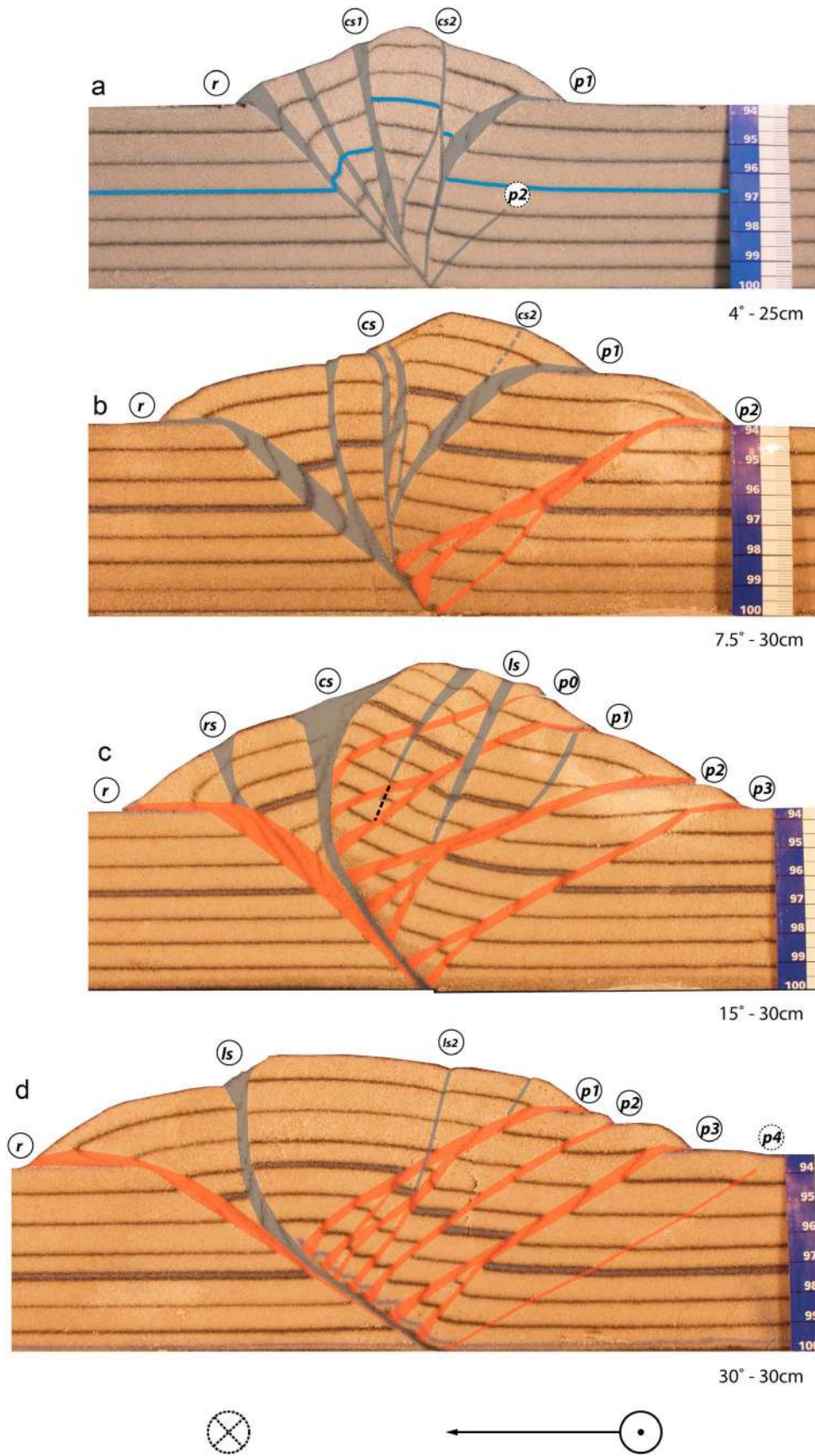
Figure 10. Effect of changing convergence angle on geometry. Cross sections for (a) 4°, (b) 7.5°, (c) 15°, and (d) 30° models (location in Figure 9).

Table 3. Kinematic Stages in Transpressional Belts[a]

Main Stage	Substage	Description
Stage 1,	*1*	*distributed strain, no discrete*
distributed strain		*faults at model surface*
Riedel	R	belt of Riedel shears
Stage 2,	*2a*	*wedge bounded by*
shear lens		*oblique slip faults*
	2b	*oblique wedge with local*
		strain partitioning on p and/or r
	2c	*oblique wedge with cs or ls*
Stage 3,	*3a*	*strain partitioning between*
strain partitioning		*strike slip on cs/ls and high*
		angle slip on p/r
	3b	*strain partitioning, r abandoned*
Strain weakening	SW	deformation on *cs* only

[a]Stages in italic font are valid for 15° reference model.

of such a fault hierarchy, the 7.5° model is transitional between the 4° model and the higher angle models. While the 4° model forms a perfect flower structure with faults branching from a common stem, all proshears in the 30° model root on the retroshear at a near-orthogonal angle, thus showing a distinct hierarchy between the retroshear and the proshears. A similar relationship between faults on the proside and retroside is observed in the 15° model, with the possible exception of $p0$ (Figure 10). In the 7.5° model, in contrast, only $p2$ (which formed during the strain partitioning stage, see below) shows a distinct hierarchical relationship with r.

4.2.2. Kinematics

[40] Through analysis of the kinematic evolution of the models, a number of structures that were common to all of the models could be defined (Table 2). However, the kinematic evolution itself, and hence the stages, proved to be different from the reference model and from each other. Therefore additional stages and substages had to be defined (Table 3 and Figures 7 and 11).

[41] The first faults to develop in the 4° model (Figure 11a), after a stage of distributed deformation (stage 1a), were an array of Riedel shears with a spacing of ~10 cm, similar to the width of the deforming wedge, and at an angle of 30 degrees to the basal velocity discontinuity (stage R). The (central segments of the) Riedel shears were later abandoned in favor of two continuous faults (r, $p1$) bounding an oblique shear lens. As soon as these were in place, a central shear zone (cs) started to develop, gradually "eating" its way southward and, in the process, abandoning fault activity on the retroside (stage 2a). After the cs assumed its final shape of a straight fault overlying and subparallel to the basal velocity discontinuity, local strain partitioning was recorded on closely spaced branches of the proshear $p1$ (stage 2b). Later, a new proshear developed ($p2$) and slip on $p1$ and $p2$ alternated between reverse and oblique (stage 3a). In the final stage of the model (stage SW) a second central shear zone developed subparallel to the imposed displacement field. The double cs accommodated all deformation in this final stage.

[42] The stages defined for the reference model (Figure 7a) are approximately valid for the 7.5° model (Figure 11b). The major difference with the reference model is that the cs evolved much earlier and the retroshear was active longer in this model (see also Figure 7b). After a period of distributed

deformation (stage 1), two well defined faults accommodating oblique displacement and bounding an uplifted wedge appeared (stage 2a). Soon after, the cs started to form by southward propagation. Strain was locally partitioned on narrowly spaced branches of $p1$ and r (stages 2b and 2c). With progressive deformation, the strike-slip branch of $p1$ evolved into a second central shear zone $cs2$. On the proside a new reverse fault formed (proshear $p2$) while deformation on the retroside continued on r and a branch l connecting r and cs (stage 2c). In the next stage (stage 3a), $cs2$, the former $p1$, was abandoned and a single CS accommodated the majority of along strike displacement. r and newly formed $p2$ accommodated mostly orthogonal displacement. Finally (stage 3b), all activity on the retroside ceased and strain was partitioned between $p2$ and cs. The latter accommodated significant uplift.

[43] The 30° model (Figure 11c) initially showed two faults with oblique displacement (stage 2a), bounding an oblique wedge like in the reference model. The width of the wedge (20 cm) was however much larger, reflecting the shallower angle of the bounding faults (Figures 10 and 8). As in the reference model, local strain partitioning developed on proside and retroside with proceeding deformation (stage 2b). The new proshears ($p2$, $p3$) developed in an en echelon arrangement rather than as parallel structures. Also equal to the reference model, this model showed a pronounced ls, here after some 13 cm displacement (stage 3a). The structures on the retroside were abandoned not long afterward (stage 3b).

[44] The initiation and active time of faults are compared for the different convergence angles in Figure 7b. For all models except the 4° model, the first faults to appear at the surface were the oblique proshears and retroshears defining the shear lens. They appeared after 3–4 cm of displacement. The first faults in the 4° model were Riedel shears and they appeared after only 2 cm of displacement. The duration of the distributed strain stage was thus longer for the higher convergence angles. A likely explanation for this is the dip of the faults, which is a function of the convergence angle. The larger convergence angles are characterized by faults with a smaller dip, which need to propagate through the sand pack over a larger distance from their nucleation point at the basal velocity discontinuity before reaching the surface.

[45] From here on, the differences between the models became more pronounced. All models formed new proshears, but their timing was very different. In the 4° model, after some 33 cm of displacement (D/h ~ 5.5) no new proshears were formed and activity ceased on the existing ones. The other models kept developing new proshears until the end of the model runs. The number of proshears and their life time were clearly dependent on the convergence angle: the 30° model developed new proshears fastest, the 4° model was slowest (see $p2$ column in Figure 7b). The 15° and 30° models have four proshears each. The 30° model would have developed the largest number of proshears if the total displacement had been equal to the other models. In contrast, the 4° and 7.5° models only developed two proshears during the entire model run (see also Figures 9 and 10). Obviously, this difference is due to the larger component of margin-perpendicular displacement with increasing convergence angle.

[46] Though the moment of initiation of the retroshear (r) was not very far apart in the different models, the length of
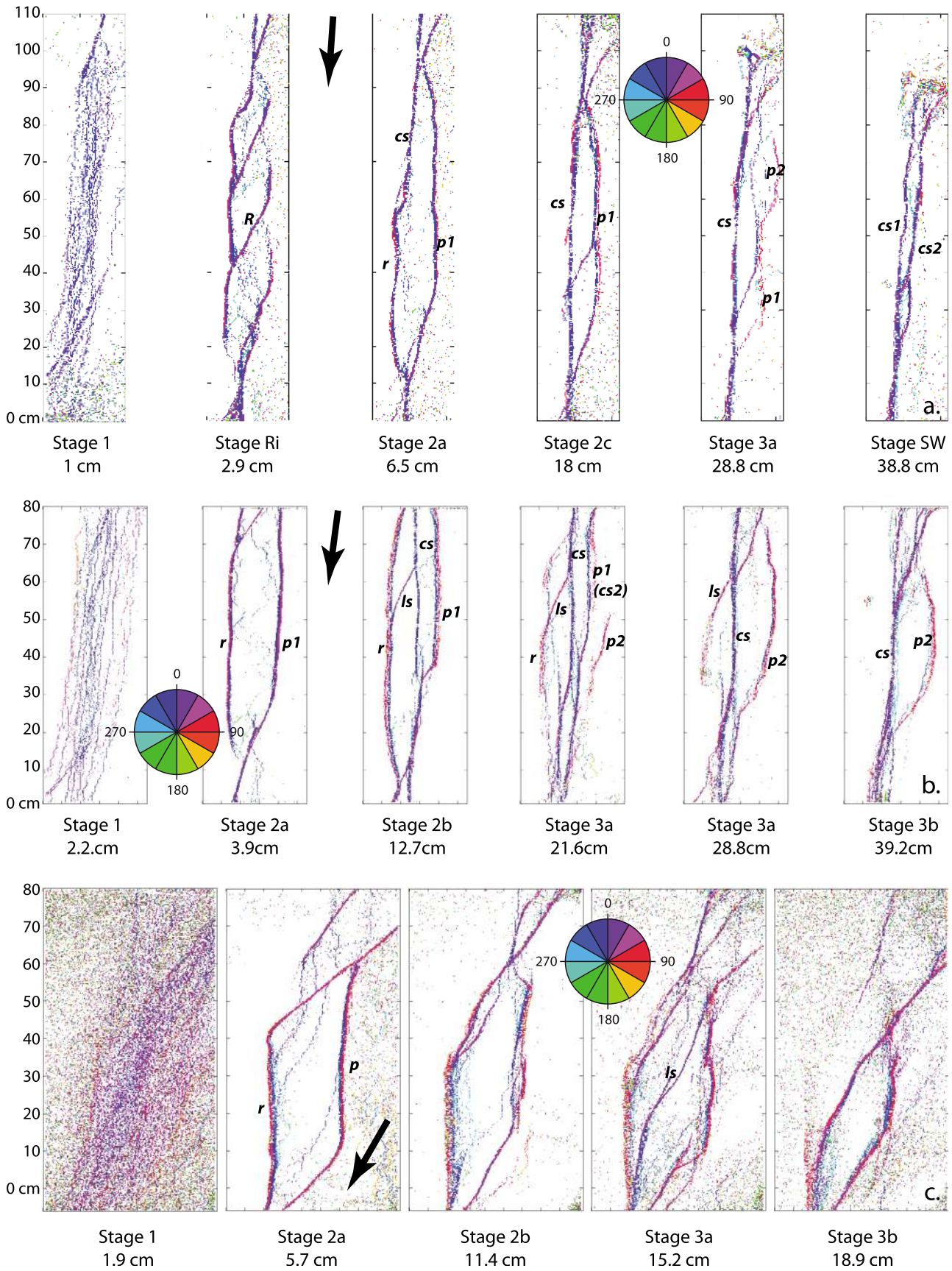
Figure 11. Fault kinematics and stages for (a) 4°, (b) 7.5°, and (c) 30° models.

the displacement interval during which it was active shows a large variation of 12 to more than 30 cm (Figure 7b). In the 4° model, it started to be replaced by the *cs* as soon as it was formed. *r* was active longest in the 7.5° model, though it did not accommodate major displacement during the final 12 cm of its existence. Its life time was intermediate in the 15° and 30° models.

[47] In the 15° and 30° models, the linking shear zone was active before the appearance of the *cs*, while in the 7.5° model, a structure geometrically similar to *ls* evolved after the *cs* had formed. The moment of appearance of the plate boundary-parallel central shear zone *cs* clearly depended on the convergence angle. For the low-angle models (7.5° and 4°) the *cs* started forming as one of the earliest structures. These models showed a double *cs*, transient in case of the 7.5° model and dominating a final and new type of deformation stage in case of the 4° model. In the 15° model, 25 cm of displacement was required for the *cs* to form. In our 30° model, which was stopped after 24 cm, a *cs* did not evolve. However, experiments by *McClay et al.* [2004] show that it will eventually develop for larger displacement.

4.2.3. Slip on Individual Fault Segments

[48] The fault kinematic analysis presented above allowed the definition of stages based on the active faults in the model and differences in fault slip based on visual analysis of the colors representing strike slip, oblique slip or dip slip. Visual inspection of these images derived from the DPIV data set only gives a rough estimate of the orientation of the fault slip vector, however, and therefore fault slip was quantified on individual fault segments (see section 3.2 and Figure 4). The results of this analysis are presented in Figures 12 and 13.

[49] The data points in the diagram of raw (unclassified) fault slip data for the reference model are rather scattered, yet two groups around 360° and 60°–75° can be identified (Figure 12a). In addition there are some data points around 300°. These groups of values were expected from the more qualitative results presented above (see Figure 6): the strike of the basal velocity discontinuity and the major faults is N−S and in this reference frame 360° corresponds to dextral strike slip, while the second group (60°–75°) corresponds to contraction with slip at a larger angle to the plate boundary. The cluster around 300° corresponds to extension or slope collapse on the steeply uplifted central prowedge.

[50] Each of the data points in this raw data set represents a pixel cluster in a fault kinematics plot (Figures 6 and 11). The pixel clusters corresponding to the main fault segments were manually identified (see section 3.2). The resulting classified data points are plotted together with the model stages defined previously in a classified fault slip diagram (Figure 12b). Here, the data points corresponding to pixel clusters that could not be attributed to one of the major faults are omitted.

[51] No faults were active in stage 1 and correspondingly, the classified plot does not show any data points in this stage (Figure 12b). In contrast, a very large number of data points, corresponding to small pixel clusters with widely varying fault slip azimuths, characterizes the raw data in this stage (Figure 12a). In stage 2a, *r* and *p0* bound the oblique wedge and feature a fault slip azimuth around 20 degrees, corresponding to highly oblique slip (Figure 12b). Stage 2b was defined by the onset of local partitioning. This is reflected in

a larger scatter of the fault slip azimuths. Slip on *r* ranges between 60° and 90°, while slip on *p1* is much more oblique (and less well constrained) with values between 30° and 70°. *rs* shows nearly pure strike slip with its slip azimuth clustering around 0°. In stage 3a *ls* became clearly expressed. Where the slip azimuth on *ls* showed a large scatter during the previous stage, it stabilized around 15° in this stage. The slip azimuth on *ls* has thus become parallel to its strike (Figures 5 and 6), confirming its dextral strike-slip character. *rs* remained a stable dextral strike-slip fault, as evidenced by the homogeneous azimuth of 0°, while *r* shows nearly perfect orthogonal contraction. In this stage, *p2* appeared. The slip vector on this fault is well constrained and shows a very distinct rotation from oblique (around 50°) during its initial activity to near orthogonal (75°–80°) at its termination. The quality of the data is not good enough to unequivocally confirm whether a similar pattern may be inferred for *p3* and even *p1*. In any case, initial slip on *p3* was again more oblique than the final movement on *p2*. During stage 3, the fault slip azimuth on *cs* changed from around 0° to 10°. A similar clockwise rotation of the strike of the fault occurred (Figure 6), showing that its dextral strike-slip character was maintained.

[52] A rather similar fault slip evolution was recorded for the 7.5° model (Figure 13a). Fault slip on *r* and *p1* in stage 2a is more oblique than in the reference model, mostly so for *p1* which shows a slip azimuth around 10°, while 15° is recorded for *r*. From the moment of its formation the *cs* accommodated progressively more displacement per time step. In this model, too, its clockwise rotation was reflected in the fault slip azimuth that increased from 0° to ~10°, as the *cs* became aligned to the displacement field. From the start of the strain partitioning stage, slip on the retroshear showed the largest angle to the plate boundary, approaching orthogonal slip like in the reference model. The magnitude of displacement on *p2* is obviously smaller than in the reference model, due to the smaller margin orthogonal component of the plate vector. Its orientation, however, shows a similar progressive clockwise rotation, increasing from oblique slip at 40° to near-orthogonal 80°.

[53] In the 4° model, finally (Figure 13b), the magnitude of reverse slip on the proshears, particularly *p2*, was generally so small that they were difficult to identify at the current resolution of our vector field. The fault identified as *p1* is a strike-slip fault rather than a reverse fault. This is also evident from its geometry in cross section (Figure 10) In this model, the strain partitioning stage (3), which is the final stage for the other models, is a transient stage. It is followed by a "strain weakening" stage characterized by rotation of the *cs* which became aligned with the applied displacement field. The fault slip azimuth diagram clearly shows the moment of rotation as the slip vector azimuth also changes from around 0° (in stages 2 and 3) to 4° (in the final strain weakening stage).

[54] The results from this new analysis allow more ready comparison between model and field data. In a companion paper [*Leever et al.*, 2011] we describe the expression of these tectonic stages in the West Spitsbergen fold and thrust belt.

4.2.4. Fault Dips

[55] In addition to the dips of the faults that characterize the final stage (Figures 8 and 10) and which show a strong
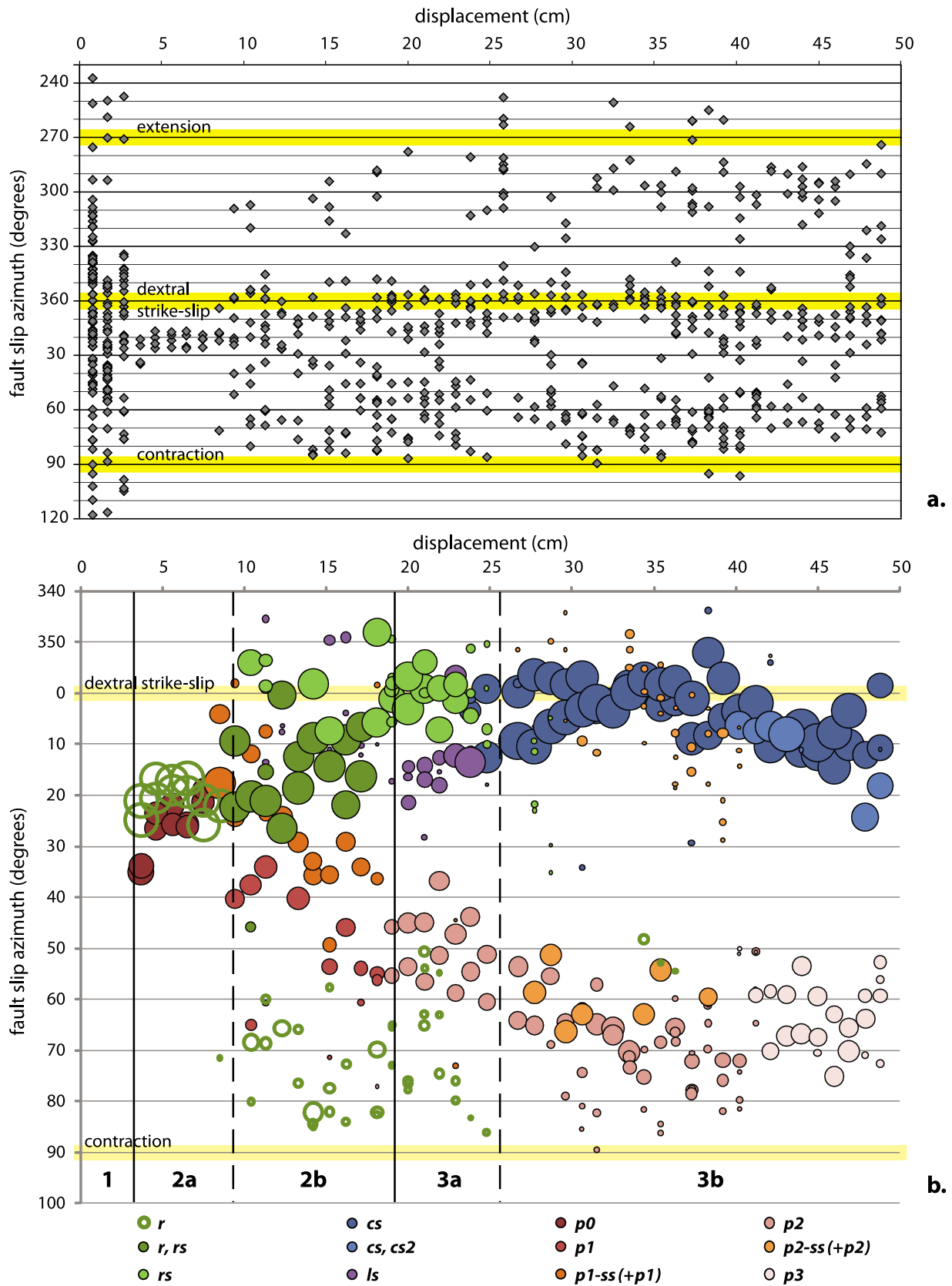
Figure 12. Fault slip azimuth versus displacement for the 15° reference model. (a) Raw data. (b) Classified data with bubble size according to average slip vector length times area. Large bubbles indicate large displacement.
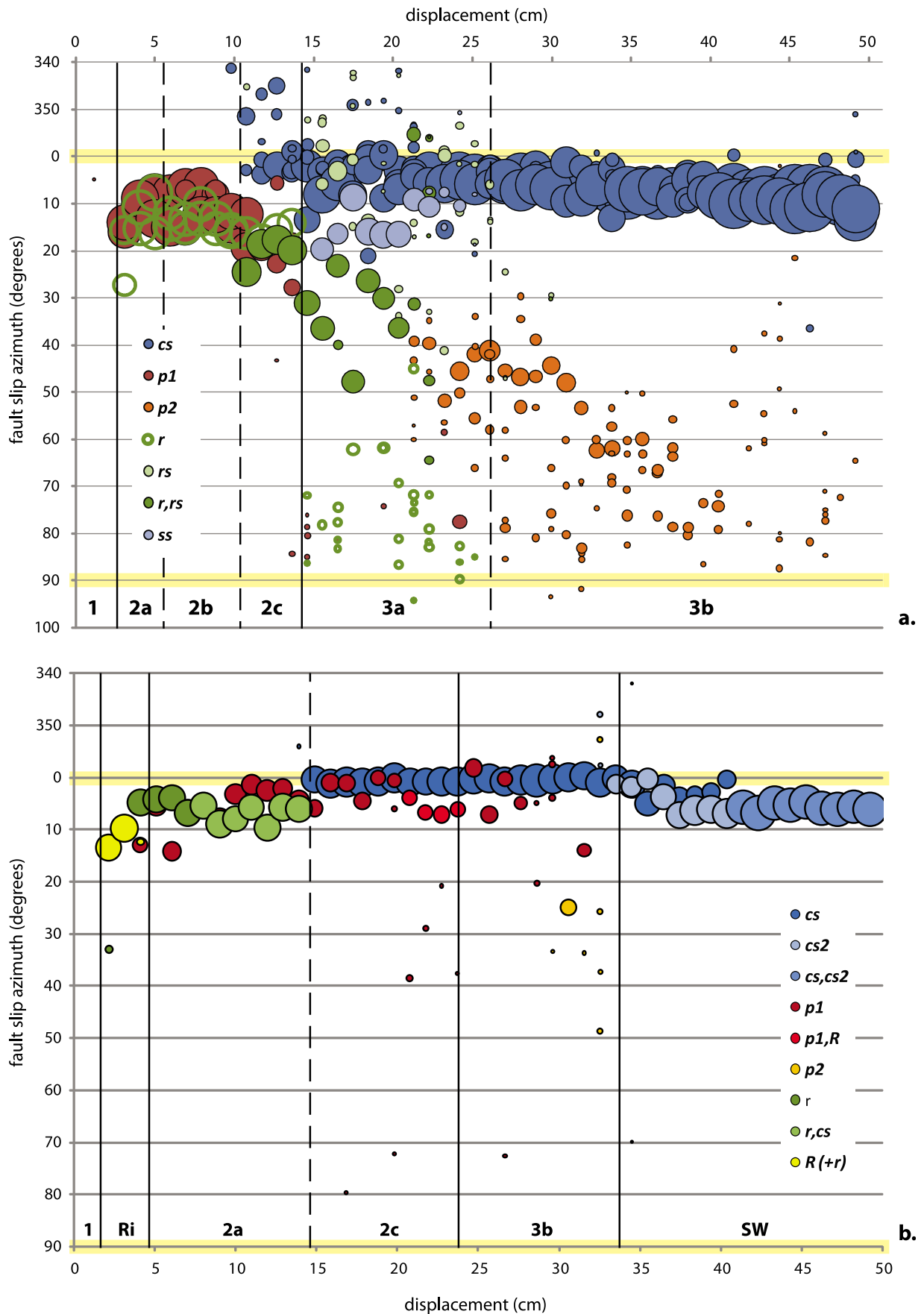
Figure 13. Fault slip azimuth versus displacement. (a) The 4° model and (b) the 7.5° model.
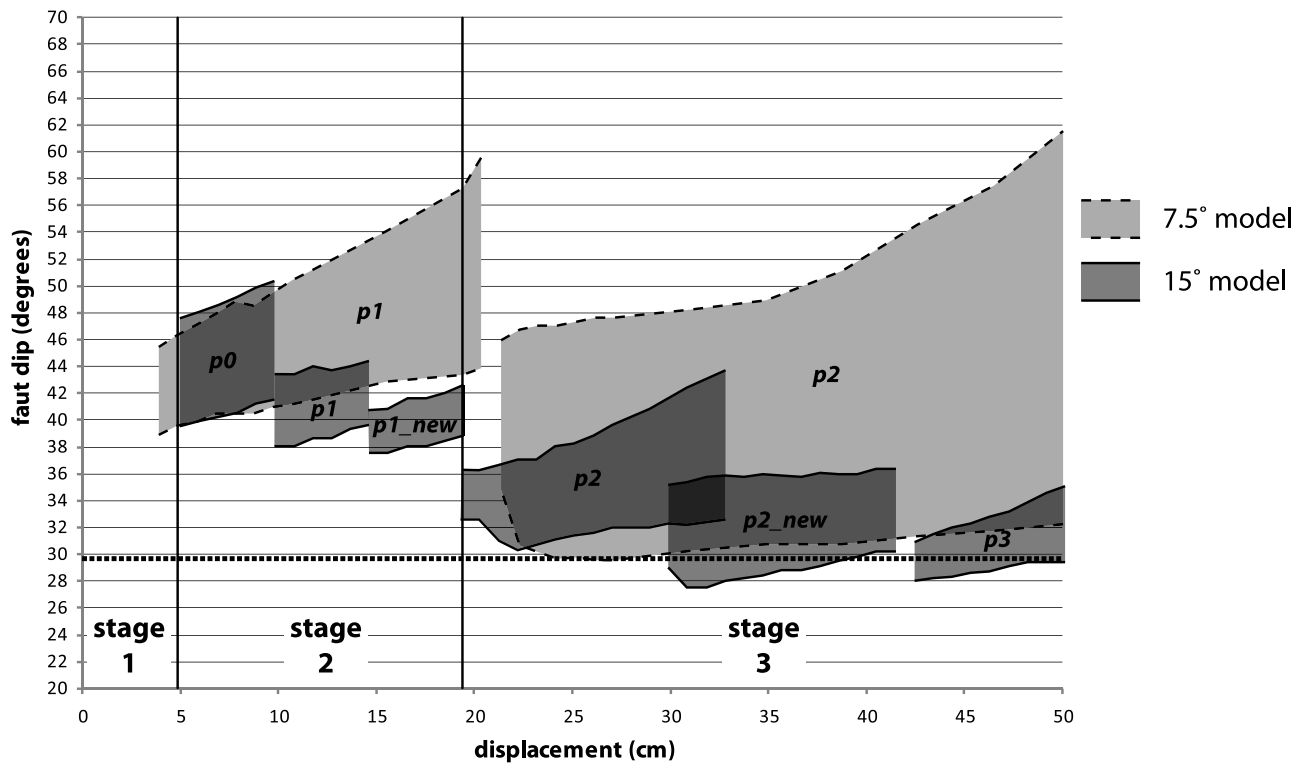
Figure 14. Fault dip evolution for 7.5° and 15° models.

correlation with convergence angle, the changing dip of the proshears with progressive displacement was measured for the two models with intermediate convergence angles (7.5° and 15°; Figure 14). The previous analyses revealed that strain partitioning is best developed in these models and this is also reflected in the fault dips. The dips were derived from the spacing between the active fault and the basal velocity discontinuity and the known height of the sand pack. The faults are not perfectly straight lines, and therefore maximum and minimum dip angles are plotted.

[56] In both models, the proshears that formed during stage 2 (*p*0 and *p*1 for the 15° model and *p*1 for the 7.5° model) initiated at a minimum dip between 40° and 37.5° (Figure 14).The initial minimum dip of the proshears formed during the strain partitioning stage (*p*2 and *p*3), in contrast, was much smaller and varied between 32° and 28°, clustering around the theoretical fault dip of 29.5° predicted by the Mohr-Coulomb failure criterion in orthogonal convergence for sand with an angle of internal friction of 31°.

[57] The increase in fault dip angle on the individual fault segments during their active time (Figure 14) is probably only apparent and reflects a translation of the prowedge (including the active fault), onto the retroshear, rather than a rotation, and thus an actual dip angle change, of the active fault. The final stage cross sections (Figure 10) support this interpretation. Where the proshears root on the retroshear (or *cs*), they consist of several closely spaced segments which merge into a single one toward the model surface. With progressive advection of the prowedge onto the retroshear, new segments are formed at the velocity discontinuity, merging with the existing upper part of the active proshear

which, while it keeps accommodating displacement, is itself also advected up the retroshear.

5. Summary of Model Results

[58] The change in model characteristics, both in terms of geometry and the kinematic evolution, is gradual between the different convergence angles. This is well expressed by the dip angle of the retroshear which gradually decreases with increasing convergence angle (Figures 8 and 10). Most of the main structural elements (*r*, *cs*, *ls*, and *p*) are common to all of the models. The 4° model is the only one with a distinct set of Riedel shears as the first faults to form (though they appeared also in some of the repeated 7.5° model runs). It also lacks a linking shear zone *ls*.

[59] Though the transitions are gradual, two groups may be defined based on similar geometries for the low-angle models (4° and 7.5°) and the higher-angle models (15° and 30°). The main characteristics of the higher-angle models are first a pronounced asymmetry with associated fault hierarchy between retroside and proside, second the presence of a *ls* in addition to a *cs* and finally a clear difference between the proshears on one hand and strike-slip faults within the prowedge and retrowedge on the other hand. The proshears root on *r* or *cs* at an angle of ~90°. In the low-angle models, faults are rather arranged as a positive flower structure with steep faults at the base, becoming less steep toward the top with convex-up geometries. Only *p*2 in the 7.5° model shows a subordinate geometry similar to the higher-angle models.

[60] Based on kinematics, however, the 7.5° and 15° models could be grouped. Both show the same kinematic stages (Table 3) and a very similar fault slip evolution (Figures 12 and 13) with a progressive clockwise rotation by ~40° of the fault slip azimuth on the proshear during the strain partitioning stage. The kinematic evolution of the 4° and 30° models does not show this behavior, though repetition of the 30° model with larger total displacement would be required to exclude this.

6. Discussion

[61] The most important previous contributions, beside field based studies, to the understanding of transpressional brittle wedges and their mechanics are given in a relatively small number of studies based on analog modeling, numerical modeling or analytical solutions [*Braun and Beaumont*, 1995; *Burbidge and Braun*, 1998; *Haq and Davis*, 2010; *Koons*, 1994; *McCaffrey*, 1992; *Platt*, 1993, 2000; *Richard and Cobbold*, 1990; *Upton et al.*, 2003; *Vernant and Chéry*, 2006]. These authors addressed the effect of convergence angle and rheology (including the strength of bounding surfaces) on initially forming structures (oblique reverse faults or strike slip), as well as on the occurrence and degree of strain partitioning during progressive deformation.

[62] This discussion will be limited to brittle frictional rheologies such as in our model wedges, and emphasize the long-term kinematic evolution of transpressional wedges and the relationship between geometry, kinematics and mechanics. The first key issue we address is the effect of convergence angle on the geometry and long-term kinematic evolution of brittle transpressional wedges, comparing our results with previous modeling results. Second, we discuss how the detailed observations of kinematics and geometry in our analog models of brittle transpressional wedges contribute to the validation of analytical mechanical models and thus to the understanding of their mechanics.

[63] A detailed comparison between analog modeling results (applying the method introduced in this paper) and the geometry and kinematics of the oblique West Spitsbergen fold and thrust belt is presented in the companion paper [*Leever et al.*, 2011].

6.1. Effect of Convergence Angle on Geometry and Kinematics

[64] The geometrical characteristics of brittle transpressional wedges vary as a function of convergence angle. This is evident from our results and has been shown as well in previous work [*Braun and Beaumont*, 1995; *Burbidge and Braun*, 1998; *McClay et al.*, 2004; *Richard and Cobbold*, 1990]. The main variables are the fault dip, reflected in the width of the wedge and the presence of a central strike-slip fault, reflecting the development of strain partitioning with long-term deformation (Figures 9–11). Our models and analyses revealed some additional characteristics which are outlined below.

[65] The previously recognized relation between convergence angle and fault dip is that a larger convergence angle corresponds to a smaller fault dip. This was theoretically predicted by *Braun and Beaumont* [1995] and has been observed in analog and numerical experiments [e.g., *Braun*

and Beaumont, 1995; *Burbidge and Braun*, 1998; *McClay et al.*, 2004]. We recorded such a relationship in our models (Figure 8). The results of *Braun and Beaumont* [1995] are in the same range. The steeper faults in our models of highly oblique convergence (4°, 7.5°) lead to a narrow wedge; for a larger convergence angle with shallow dipping faults (30°), the wedge is correspondingly wider (Figures 9 and 10).

[66] In addition, we were able to establish a relation between the fault dip and the kinematic stage of the wedge. Proshears that formed during the strain partitioning stage have a smaller dip than the ones formed for the same convergence angle but during the oblique wedge stage (Figure 14). In addition, they show a subordinate relationship to the retro (or central) shear zone upon which they root at a high angle. This is best expressed in the 7.5° model, in which the geometries of $p1$ and $p2$ in relation to the central shear zone are very different (Figure 10). The faults formed during the oblique wedge stage (r, cs, $p1$) are arranged as a positive flower structure with steep dips at the base, becoming less steep toward the top with convex-up geometries. In contrast, $p2$ shows a very different geometry, subordinate to r/cs by rooting on it at a high angle. In the 15° model, which also demonstrated very well developed strain partitioning, the difference in dip between the latest proshears and the retroshear is more telling (Figures 8 and 10). In this model (and also in the 7.5° model), the retroshear shows a consistently larger dip than the latest proshear, formed during strain partitioning. In contrast to the proshears, which are transient structures and may adapt to the prevalent stress regime, the retroshear is a long-lived and stable feature and its dip does not change even if fault slip does. For comparison, the dip of proshears and retroshears is approximately equal for the 30° model, which never grew out of the oblique wedge stage.

[67] This means that the wedge geometry is influenced not only by the externally imposed convergence angle, but also by the kinematic stage of the wedge which changes the "apparent" convergence angle. Based on the wedge geometry and fault hierarchy, two groups could be defined, one for the high angle (15°, 30°) and one for the low-angle (4°, 7.5°) models.

6.2. Inferences on Transpressional Brittle Wedge Mechanics

[68] Two important characteristics of (brittle) transpressional wedges have been predicted by analytical models. The first one concerns the initial stage of wedge evolution and distinguishes "wrench-dominated" and "pure shear-dominated" transpression [*Burbidge and Braun*, 1998; *Tikoff and Teyssier*, 1994]. The second one concerns the strain partitioning stage and predicts a constant slip vector azimuth at the front, as a function of internal friction and/or friction on the bounding surfaces of the wedge [*Haq and Davis*, 2010; *McCaffrey*, 1992; *Platt*, 1993]. Both are discussed below in the light of our model results.

6.2.1. Initial Development: First Faults

[69] Differences in the initial evolution of transpressional wedges as a function of convergence angle have been attributed to the changing orientation of the stress triad with convergence obliquity [*Burbidge and Braun*, 1998; *Fossen and Tikoff*, 1993; *Koons*, 1994]. We define a reference

frame in which x and y are both horizontal and perpendicular and parallel to the plate boundary, respectively, and z is vertical. For orthogonal convergence, $\sigma1$ // x, $\sigma2$ // y and $\sigma3$ // z, while in strike slip, $\sigma1$ and $\sigma3$ are horizontal and at an angle of 45° to x and y, and $\sigma2$ // z. To explain these end-member orientations of the stress triad and predict the intermediate ones, it has been proposed that the stress triad rotates around the vertical (σz) axis with increasing obliquity [*Burbidge and Braun*, 1998; *Tikoff and Teyssier*, 1994]. With increasing obliquity, the relative magnitude of $\sigma2$ and $\sigma3$ also changes, the difference between them becoming smaller. At a convergence angle of 20°, $\sigma2$ and $\sigma3$ change position: $\sigma2$ is vertical from now on. The convergence angle of 20° thus marks the transition between wrench-dominated transpression and pure shear-dominated transpression [*Fossen et al.*, 1994; *Tikoff and Teyssier*, 1994]. Alternatively, *Koons* [1994] proposed a change of the shear stress τ_{xy} as a function of the convergence angle and a rotation of the principal stresses around the *x* axis. His model assumes a wedge with a sloping top and base and thus represents a 3-D case of the 2-D critical wedge model [*Dahlen*, 1984; *Davis et al.*, 1983; *Lehner*, 1986]. In this case the initial orientation of $\sigma1$ is not horizontal but it may have a dip of up to 40° in the x direction.

[70] What are the implications of these different transpression regimes? According to the theory, the initially forming structures should be (vertical) strike-slip faults for convergence angles ≤ 20 degrees, and reverse faults above 20 degrees [*Tikoff and Teyssier*, 1994]. In transtension, this theoretical angle was confirmed by experimental results [*Withjack and Jamison*, 1986]. This concept of "first faults," however, is not exactly reproduced by analog models of transpressional wedges. Typically, even in the wrench-dominated regime, an oblique wedge forms before a strike-slip fault evolves above the basal velocity discontinuity (see the 15° and 7.5° models; Figures 6 and 11b). Only in case of the very lowest convergence angles (<5°) a strike-slip fault is the first to form (see the Riedel shears in the 4° model; Figure 11a). This is the case both for brittle (our results) [see also *Burbidge and Braun*, 1998; *Richard and Cobbold*, 1990] and brittle-ductile [*Casas et al.*, 2001; *Richard and Cobbold*, 1990] rheologies.

[71] *Tikoff and Teyssier* [1994] give a possible explanation for this discrepancy by emphasizing the importance of the kinematic boundary conditions in controlling deformation, rather than stresses. In other words, if the behavior of the brittle model wedges is different from theory, it is because the orientation of the stress triad may be strongly affected by kinematic boundary conditions, in our case the linear basal velocity discontinuity (VD). Faults are prone to nucleate at this VD and hence the localization and orientation of the first faults at depth will be determined by it. In strike-slip systems with a basal VD, the plough shape of Riedel shears is explained by a change of the orientation of the stress triad with depth [*Naylor et al.*, 1986]. At the free surface, the stress triad is oriented with $\sigma2$ vertical, and $\sigma1$ and $\sigma3$ horizontal and at 45° to the VD. Strike slip faults then form at an orientation to the VD determined by the Mohr-Coulomb failure criterion, in the same way as they would in response to far-field stress in this orientation. However, with depth the influence of the VD becomes more pronounced. Thus, for the smallest convergence angles in a

transpressional system, the changing orientation of the stress tensor with depth leads to the development of R, R' and P shears, forming a positive flower structure [*Tchalenko and Ambrasyas*, 1970; *Christie-Blick and Biddle*, 1985].

[72] In the brittle upper crust, a velocity discontinuity such as in our experimental setup may result from any rheological or geometric irregularity which was present at the onset of shortening. For example, along a large normal fault bounding a half graben or in inherited negative flower structures basement rocks could be juxtaposed with weaker sedimentary rocks. At a larger scale, a plate boundary oriented oblique to the direction of plate motion will form a (possibly sharp) oblique velocity discontinuity.

6.2.2. Strain Partitioning Stage: Fault Slip at the Front

[73] Strain partitioning is a phenomenon that only develops after relatively long-term deformation, as has been recorded before [*Burbidge and Braun*, 1998; *McClay et al.*, 2004] and is confirmed by our results. The previous discussion on the orientation of the stress triad refers to initially forming structures only, and is not valid for large deformation because the topographic buildup perturbs the initial layer cake geometry and creates a true doubly vergent wedge.

[74] Analytical models of fore-arc slivers / oblique subduction/transpressional wedges have been used to study the relation between bulk rheology of accretionary wedges and the degree of strain partitioning [*Haq and Davis*, 2010; *McCaffrey*, 1992; *Platt*, 1993, 2000]. The analytical models are mostly defined for accretionary wedges at obliquely convergent subduction zones. Three different classes of brittle/frictional wedge models are recognized, with increasing complexity.

[75] 1. The simplest model is that of a block bounded by a horizontal plane at the base and vertical plane at the back [*Haq and Davis*, 2010]. This block represents a fore-arc sliver and is not allowed to deform internally.

[76] 2. A second model representing oblique subduction zones is that of a critical wedge with a sloping base and a vertical fault at the back [*McCaffrey*, 1992; *Platt*, 1993].

[77] 3. The third model represents continent-continent collision. In this model, which is based on the work by *McCaffrey* [1992], the dip of lower surface (Δ) is a function of convergence angle α and not an independent variable like in the previous two models [*Burbidge and Braun*, 1998]. This case is representative for our models.

[78] The first two models have shown that wedges with perfectly plastic and Coulomb brittle rheologies behave similarly in oblique convergence: strain will be partitioned when the convergence angle exceeds a critical obliquity [*Haq and Davis*, 2010; *Platt*, 1993]. During strain partitioning, there is a maximum slip obliquity at the front which is a function of the friction on the boundaries of the wedge and which is independent of plate convergence angle [*Haq and Davis*, 2010; *McCaffrey*, 1992; *Platt*, 1993]. As a consequence, the degree of strain partitioning (i.e., the fraction of margin parallel slip accommodated on the strike-slip fault) increases as the convergence angle decreases, giving the trivial result that pure strike-slip margins show the highest degree of strain partitioning. The third approach was used only to derive the critical convergence angle for strain partitioning.

[79] Since the previous quantitative analytical work focused on steady state conditions, the results should be compared with our strain partitioning stage only. Our model

results disagree with the prediction of constant slip obliquity at the front for accretionary wedges [*Haq and Davis*, 2010; *McCaffrey*, 1992]. On a single proshear (*p2* in 7.5° and 15° experiments) a rotation of the slip vector by up to 40 degrees has been recorded (Figures 12 and 13). A potential cause for this rotation of the slip vector on the frontal reverse fault could be the progressive topographic buildup. In initially nonpartitioned systems, the late-stage evolution of strain partitioning by formation of a central strike-slip fault has been attributed to increase in topography, which in turn changes the force balance within the wedge by increasing the vertical component of the stress tensor [*Burbidge and Braun*, 1998]. An additional contribution may come from deactivation of other faults in the wedge (e.g., the retroshear) so that a larger component of the margin orthogonal slip is accommodated by the frontal proshear. If topography indeed is a key control on fault kinematics, the effect of erosion should be investigated. Previous studies of 2-D (orthogonal) orogenic wedges have proven the impact of erosion on wedge dynamics [*Willett et al.*, 1993] and there is no reason to assume it will be less so in 3D [*Koons*, 1994].

[80] A direct comparison between the analytical solutions of *Platt* [1993], *McCaffrey* [1992], *Haq and Davis* [2010] and our model results may not be possible because of the different boundary conditions. These analytical models represent accretionary wedges / fore-arc slivers on oceanic subduction zones. An important characteristic of these is that the dip of the basal surface (β) is independent of the convergence obliquity. In our models, representing continent-continent collision, the dip of the frontal reverse fault is a function of the convergence angle. In addition, it changes with the progressive evolution of the wedge: proshears formed during strain partitioning stage have lower dips than initial faults.

[81] The degree of strain partitioning in our models increases during progressive slip on a single fault. This behavior could possibly be compared with a dynamic steady state such as the out-of-sequence thrusting in a brittle wedge after the formation of a new thrust at the toe, in order to maintain the critical taper [*Davis et al.*, 1983]. Based on our observations we cannot decide that the analytical results are not valid for brittle continent-continent wedges, but if one wants to make prediction about bulk wedge rheology based on kinematic observations [e.g., *Platt*, 2000], behavior deviating from steady state must be taken into account.

7. Conclusions

[82] We used a high-resolution image analysis technique (DPIV) to monitor and analyze in unprecedented detail the long-term kinematic evolution of transpressional brittle wedges as a function of convergence angle. The analysis focused on the occurrence (including initiation and expression) and degree of strain partitioning during highly oblique convergence. The DPIV results moreover allowed the validation of analytical models of transpressional wedge mechanics, particularly the following.

[83] 1. The change in geometric characteristics of transpressional brittle wedges as a function of convergence angle is gradual. The highest obliquities (4°, 7.5° convergence angle) are characterized by the narrowest deformation zone and steepest faults, which are arranged in a flower structure.

The lower obliquities (15° and 30° convergence angles) are characterized by lower fault dip angles and consequently wider wedges and feature a distinct fault hierarchy in which the proshears are subordinate to and root at a high angle on a longer-lived retroshear.

[84] 2. The kinematic evolution of transpressional brittle wedges is characterized by a sequence of distinct stages, culminating in a stage of strain partitioning. Remarkably, these stages develop for constant kinematic boundary conditions (i.e., convergence angle and displacement rate) and a uniform brittle rheology and occur consistently in the realm of convergence angles between 4 and 30 degrees. Three distinct kinematic stages could be defined for the models with 7.5° and 15° convergence angles. These are an initial "distributed strain" stage during which no faults appear at the model surface, a second "oblique wedge" stage with oblique slip on the faults bounding the wedge on proside and retroside. In the course of this stage, slip becomes locally partitioned on strike-slip and reverse faults branching from the master fault which still accommodates oblique slip at depth. In the "strain partitioning stage" strain is partitioned between plate boundary parallel slip on a large strike-slip fault in the center of the wedge and slip at a high angle to the plate boundary on the bounding faults. The 4° model features an additional stage at the start, in which Riedel shears are active.

[85] 3. The previously established relationship between convergence angle and fault dip angle was confirmed. In addition, a relationship was established between the kinematic stage and fault dip angle. Proshears that formed during the strain partitioning stage evolved at a smaller dip (approaching that for orthogonal convergence) than the proshears that formed during the oblique wedge stage.

[86] 4. Determination of the fault slip azimuth on individual fault segments for the 7.5° and 15° models revealed that the slip vector on the proshears during the strain partitioning stage is not constant but rotates by up to 40° from initially oblique to nearly pure reverse. This may be explained by topographic buildup increasing the vertical stress, strain weakening of the faults or possibly changes in slip rates on other fault segments. Further analysis is required to resolve this and the implications, i.e., whether it means that the degree of strain partitioning indeed is not constant for a constant angle of plate convergence, as has been predicted by analytical models.

Notation

α angle of plate convergence
α' convergence obliquity ($90 - \alpha$)
δ fault dip in the direction of maximum principal stress σ_1
Δ fault dip perpendicular to plate boundary / basal velocity discontinuity
θ angle between maximum principal stress σ_1 and the normal to plate boundary
φ angle of internal friction (31° for dry quartz sand)
ψ critical slip obliquity
ρ density
σ stress

References

Adam, J., J. L. Urai, B. Wieneke, O. Oncken, K. Pfeiffer, N. Kukowski, J. Lohrmann, S. Hoth, W. van der Zee, and J. Schmatz (2005), Shear localisation and strain distribution during tectonic faulting—New insights from granular-flow experiments and high-resolution optical image correlation techniques, *J. Struct. Geol.*, *27*, 283–301, doi:10.1016/j.jsg.2004.08.008.

Beaumont, C., P. Fullsack, and J. Hamilton (1994), Styles of crustal deformation in compressional orogens caused by subduction of the underlying lithosphere, *Tectonophysics*, *232*(1–4), 119–132, doi:10.1016/0040-1951(94)90079-5.

Bonini, M., D. Sokoutis, G. Mulugeta, and E. Kartrivanos (2000), Modelling hanging wall accommodation above rigid thrust ramps, *J. Struct. Geol.*, *22*, 1165–1179, doi:10.1016/S0191-8141(00)00033-X.

Braun, J., and C. Beaumont (1995), Three-dimensional numerical experiments of strain partitioning at oblique plate boundaries: Implications for contrasting tectonic styles in the southern Coast Ranges, California, and central South Island, New Zealand, *J. Geophys. Res.*, *100*(B9), 18,059–18,074, doi:10.1029/95JB01683.

Burbidge, D. R., and J. Braun (1998), Analogue models of obliquely convergent continental plate boundaries, *J. Geophys. Res.*, *103*(B7), 15,221–15,237, doi:10.1029/98JB00751.

Burov, E. (2007), Plate rheology and mechanics, in *Crustal and Lithosphere Dynamics*, edited by A. B. Watts, pp. 99–151, doi:10.1016/B978-044452748-6/00102-4, Elsevier, Amsterdam.

Byerlee, J. (1978), Friction of rocks, *Pure Appl. Geophys.*, *116*(4–5), 615–626, doi:10.1007/BF00876528.

Casas, A. M., D. Gapais, T. Nalpas, K. Besnard, and T. Román-Berdiel (2001), Analogue models of transpressive systems, *J. Struct. Geol.*, *23*, 733–743, doi:10.1016/S0191-8141(00)00153-X.

Christie-Blick, N., and K. T. Biddle (1985), Deformation and basin formation along strike-slip faults, in *Strike-Slip Deformation, Basin Formation and Sedimentation*, edited by N. Christie-Blick and K. T. Biddle, pp. 79–103, Soc. of Econ. Mineral. and Palaeontol., Tulsa, Okla.

Dahlen, F. A. (1984), Noncohesive critical Coulomb wedges: An exact solution, *J. Geophys. Res.*, *89*(B12), 10,125–10,133, doi:10.1029/JB089iB12p10125.

Davis, D., J. Suppe, and F. A. Dahlen (1983), Mechanics of fold-and-thrust belts and accretionary wedges, *J. Geophys. Res.*, *88*(B2), 1153–1172, doi:10.1029/JB088iB02p01153.

Del Castello, M., K. R. McClay, and G. A. Pini (2005), Role of preexisting topography and overburden on strain partitioning of oblique doubly vergent convergent wedges, *Tectonics*, *24*, TC6004, doi:10.1029/2005TC001816.

Fitch, T. J. (1972), Plate convergence, transcurrent faults, and internal deformation adjacent to Southeast Asia and the western Pacific, *J. Geophys. Res.*, *77*(23), 4432–4460, doi:10.1029/JB077i023p04432.

Fossen, H., and B. Tikoff (1993), The deformation matrix for simultaneous simple shearing, pure shearing and volume change, and its application to transpression/transtension tectonics, *J. Struct. Geol.*, *15*, 413–422, doi:10.1016/0191-8141(93)90137-Y.

Fossen, H., B. Tikoff, and C. Teyssier (1994), Strain modeling of transpressional and transtensional deformation, *Nor. Geol. Tidsskr.*, *74*(3), 134–145.

Goetze, C., and B. Evans (1979), Stress and temperature in the bending lithosphere as constrained by experimental rock mechanics, *Geophys. J. R. Astron. Soc.*, *59*(3), 463–478.

Haq, S. S. B., and D. M. Davis (2009), Interpreting finite strain: Analysis of deformation in analog models, *J. Struct. Geol.*, *31*, 654–661, doi:10.1016/j.jsg.2009.03.017.

Haq, S. S. B., and D. M. Davis (2010), Mechanics of fore-arc slivers: Insights from simple analog models, *Tectonics*, *29*, TC5015, doi:10.1029/2009TC002583.

Hubbert, M. K. (1937), Theory of scale models as applied to the study of geologic structures, *Geol. Soc. Am. Bull.*, *48*, 1459–1520.

Jamison, W. R. (1991), Kinematics of compressional fold development in convergent wrench terranes, *Tectonophysics*, *190*(2–4), 209–232, doi:10.1016/0040-1951(91)90431-Q.

Jones, R. R., and P. W. G. Tanner (1995), Strain partitioning in transpression zones, *J. Struct. Geol.*, *17*, 793–802, doi:10.1016/0191-8141(94)00102-6.

Kirby, S. H. (1983), Rheology of the lithosphere, *Rev. Geophys.*, *21*(6), 1458–1487, doi:10.1029/RG021i006p01458.

Koons, P. O. (1994), Three-dimensional critical wedges: Tectonics and topography in oblique collisional orogens, *J. Geophys. Res.*, *99*(B6), 12,301–12,315, doi:10.1029/94JB00611.

Koons, P. O., and C. M. Henderson (1995), Geodetic analysis of model oblique collision and comparison to the Southern Alps of New Zealand, *N. Z. J. Geol. Geophys.*, *38*, 545–552, doi:10.1080/00288306.1995.9514681.

Lallemand, S., C.-S. Liu, S. Dominguez, P. Schnürle, J. Malavieille, and the ACT Scientific Crew (1999), Trench-parallel stretching and folding of forearc basins and lateral migration of the accretionary wedge in the southern Ryukyus: A case of strain partition caused by oblique convergence, *Tectonics*, *18*, 231–247, doi:10.1029/1998TC900011.

Leever, K. A., R. H. Gabrielsen, J. I. Faleide, and A. Braathen (2011), A transpressional origin for the West Spitsbergen fold-and-thrust belt: Insight from analogue modeling, *Tectonics*, doi:10.1029/2010TC002753, in press.

Lehner, F. K. (1986), Comments on "Noncohesive critical Coulomb wedges: An exact solution" by F. A. Dahlen, *J. Geophys. Res.*, *91*(B1), 793–796, doi:10.1029/JB091iB01p00793.

Lowell, J. D. (1972), Spitsbergen Tertiary orogenic belt and the Spitsbergen fracture zone, *Geol. Soc. Am. Bull.*, *83*, 3091–3102, doi:10.1130/0016-7606(1972)83[3091:STOBAT]2.0.CO;2.

Maher, H. D., and C. Craddock (1988), Decoupling as an alternate model for transpression during the initial opening of the Norwegian-Greenland Sea, *Polar Res.*, *6*(1), 137–140, doi:10.1111/j.1751-8369.1988.tb00590.x.

McCaffrey, R. (1992), Oblique plate convergence, slip vectors, and forearc deformation, *J. Geophys. Res.*, *97*(B6), 8905–8915, doi:10.1029/92JB00483.

McClay, K. R., P. S. Whitehouse, T. Dooley, and M. Richards (2004), 3D evolution of fold and thrust belts formed by oblique convergence, *Mar. Pet. Geol.*, *21*(7), 857–877, doi:10.1016/j.marpetgeo.2004.03.009.

Naylor, M. A., G. Mandl, and C. H. K. Sijpestijn (1986), Fault geometries in basement-induced wrench faulting under different initial stress states, *J. Struct. Geol.*, *8*, 737–752.

Pinet, N., and P. R. Cobbold (1992), Experimental insights into the partitioning of motion within zones of oblique subduction, *Tectonophysics*, *206*(3–4), 371–388, doi:10.1016/0040-1951(92)90388-M.

Platt, J. P. (1993), Mechanics of oblique convergence, *J. Geophys. Res.*, *98*(B9), 16,239–16,256, doi:10.1029/93JB00888.

Platt, J. P. (2000), Calibrating the bulk rheology of active obliquely convergent thrust belts and forearc wedges from surface profiles and velocity distributions, *Tectonics*, *19*, 529–548, doi:10.1029/1999TC001121.

Polonia, A., L. Torelli, G. Brancolini, and M. -F. Loreto (2007), Tectonic accretion versus erosion along the southern Chile trench: Oblique subduction and margin segmentation, *Tectonics*, *26*, TC3005, doi:10.1029/2006TC001983.

Ranalli, G. (1997), Rheology of the lithosphere in space and time, *Geol. Soc. Spec. Publ.*, *121*(1), 19–37.

Richard, P., and P. R. Cobbold (1990), Experimental insights into partitioning of fault motions in continental convergent wrench zones, *Ann. Tecton.*, *4*(2), 35–44.

Riedel, W. (1929), Zur Mechanik geologischer Brucherscheinungen, *Centralbl. Mineral. Geol. Palaeontol.*, *1929B*, 354–368.

Sanderson, D. J., and W. R. D. Marchini (1984), Transpression, *J. Struct. Geol.*, *6*, 449–458, doi:10.1016/0191-8141(84)90058-0.

Schellart, W. P. (2000), Shear test results for cohesion and friction coefficients for different granular materials: Scaling implications for their usage in analogue modelling, *Tectonophysics*, *324*(1–2), 1–16, doi:10.1016/S0040-1951(00)00111-6.

Schreurs, G., and B. Colletta (1998), Analogue modelling of faulting in zones of continental transpression and transtension, in *Continental Transpressional and Transtensional Tectonics*, edited by R. E. Holdsworth, R. A. Strachan, and J. F. Dewey, *Geol. Soc. Spec. Publ.*, *135*, 59–79.

Sibson, R. H. (1974), Frictional constraints on thrust, wrench and normal faults, *Nature*, *249*(5457), 542–544, doi:10.1038/249542a0.

Sveen, J. K. (2004), *An Introduction to MatPIV v. 1.6.1*, [electronic], *Mechanics and Applied Mathematics*, vol. 2, Dep. of Math., Univ. of Oslo, Oslo.

Tchalenko, J. S., and N. N. Ambraseys (1970), Structural analysis of the Dasht-e Bayaz (Iran) earthquake fractures, *Geol. Soc. Am. Bull.*, *81*, 41–60, doi:10.1130/0016-7606(1970)81[41:SAOTDB]2.0.CO;2.

Teyssier, C., B. Tikoff, and M. Markley (1995), Oblique plate motion and continental tectonics, *Geology*, *23*(5), 447–450, doi:10.1130/0091-7613(1995)023<0447:OPMACT>2.3.CO;2.

Tikoff, B., and H. Fossen (1993), Simultaneous pure and simple shear: The unifying deformation matrix, *Tectonophysics*, *217*(3–4), 267–283, doi:10.1016/0040-1951(93)90010-H.

Tikoff, B., and C. Teyssier (1994), Strain modeling of displacement-field partitioning in transpressional orogens, *J. Struct. Geol.*, *16*, 1575–1588, doi:10.1016/0191-8141(94)90034-5.

Titus, S. J., B. Housen, and B. Tikoff (2007), A kinematic model for the Rinconada fault system in central California based on structural analysis of en echelon folds and paleomagnetism, *J. Struct. Geol.*, *29*, 961–982, doi:10.1016/j.jsg.2007.02.004.

Upton, P., P. O. Koons, and D. Eberhart-Phillips (2003), Extension and partitioning in an oblique subduction zone, New Zealand: Constraints from three-dimensional numerical modeling, *Tectonics*, *22*(6), 1068, doi:10.1029/2002TC001431.

Vernant, P., and J. Chéry (2006), Mechanical modelling of oblique convergence in the Zagros, Iran, *Geophys. J. Int.*, *165*(3), 991–1002, doi:10.1111/j.1365-246X.2006.02900.x.

Weinberger, R., M. R. Gross, and A. Sneh (2009), Evolving deformation along a transform plate boundary: Example from the Dead Sea Fault in northern Israel, *Tectonics*, *28*, TC5005, doi:10.1029/2008TC002316, doi:10.1029/2008TC002316.

Westerweel, J. (1993), Digital particle image velocimetry, Ph.D. thesis, 237 pp., Delft Univ. of Technol., Delft, Netherlands.

Willett, S., C. Beaumont, and P. Fullsack (1993), Mechanical model for the tectonics of doubly vergent compressional orogens, *Geology*, *21*(4), 371–374, doi:10.1130/0091-7613(1993)021<0371:MMFTTO>2.3.CO;2.

Withjack, M. O., and W. R. Jamison (1986), Deformation produced by oblique rifting, *Tectonophysics*, *126*(2–4), 99–124, doi:10.1016/0040-1951(86)90222-2.

Yu, G., S. G. Wesnousky, and G. Ekström (1993), Slip partitioning along major convergent plate boundaries, *Pure Appl. Geophys.*, *140*(2), 183–210, doi:10.1007/BF00879405.

R. H. Gabrielsen, Department of Geosciences, University of Oslo, PO Box 1047 Blindern, N-0316 Oslo, Norway. (r.h.gabrielsen@geo.uio.no)

K. A. Leever, Department of Lithosphere Dynamics, Deutsches GeoForschungsZentrum, Telegrafenberg, D-14473 Potsdam, Germany. (karen.leever@gfz-potsdam.de)

D. Sokoutis and E. Willingshofer, Faculty of Earth- and Life Sciences, VU University of Amsterdam, de Boelelaan 1085, NL-1081 HV Amsterdam, Netherlands. (dimitrios.sokoutis@falw.vu.nl; ernst.willingshofer@falw.vu.nl)